



AMERICAN METEOROLOGICAL SOCIETY

Journal of Physical Oceanography

EARLY ONLINE RELEASE

This is a preliminary PDF of the author-produced manuscript that has been peer-reviewed and accepted for publication. Since it is being posted so soon after acceptance, it has not yet been copyedited, formatted, or processed by AMS Publications. This preliminary version of the manuscript may be downloaded, distributed, and cited, but please be aware that there will be visual differences and possibly some content differences between this version and the final published version.

The DOI for this manuscript is doi: 10.1175/JPO-D-15-0197.1

The final published version of this manuscript will replace the preliminary version at the above DOI once it is available.

If you would like to cite this EOR in a separate work, please use the following full citation:

Jones, C., and P. Cessi, 2016: Interbasin transport of the meridional overturning circulation. *J. Phys. Oceanogr.* doi:10.1175/JPO-D-15-0197.1, in press.

© 2016 American Meteorological Society



Interbasin transport of the meridional overturning circulation

C. S. Jones* and Paola Cessi

Scripps Institution of Oceanography, University of California, San Diego

*Corresponding author address: C. S. Jones,

Scripps Institution of Oceanography,

University of California, San Diego,

La Jolla, CA 92039-0213.

E-mail: csjones@ucsd.edu

ABSTRACT

9 The meridional overturning circulation (MOC) is studied in an idealized do-
10 main with two basins connected by a circumpolar channel in the southernmost
11 region. Flow is forced at the surface by longitude-independent wind-stress,
12 freshwater flux and fast temperature relaxation to prescribed profiles. The
13 only longitudinal asymmetry is that one basin is twice as wide as the other.
14 Two states, a preferred one with sinking in the narrow basin, and an asymmet-
15 rically forced one with sinking in the wide basin, are compared. In both cases,
16 sinking is compensated by upwelling everywhere else, including the passive
17 basin. Despite the greater area of the wide basin, the residual overturning
18 transport is the same regardless of the location of sinking. The two basins ex-
19 change flow at their southern edge by a geostrophic transport balanced by the
20 difference in the depth of isopycnals at the eastern boundaries of each basin.
21 Gnanadesikan (1999)'s model for the upper branch of the MOC is extended to
22 include two basins connected by a re-entrant channel and is used to illustrate
23 the basic properties of the flow: the layer containing the surface and inter-
24 mediate water is shallower in the active basin than in the passive basin, and
25 this difference geostrophically balances an exchange flow from the passive to
26 the active basin. The exchange flow is larger when sinking occurs in the nar-
27 row basin. A visualization of the horizontal structure of the upper branch of
28 the MOC shows that both the gyres and the meridional flow are important in
29 determining the flow field.

30 **1. Introduction**

31 In the current climate system, deep water is formed in the North Atlantic, but not in the North
32 Pacific, resulting in a global meridional overturning circulation (MOC) which transports heat
33 northward in the Atlantic and contributes to a more marked southward heat flux in the South
34 Indo-Pacific. The MOC is a global cell, driven by the wind-induced upwelling in the circumpolar
35 region (Toggweiler and Samuels 1993; Wolfe and Cessi 2010), as well as by diffusive upwelling at
36 the interface between the deep and abyssal waters (Stommel and Arons 1959; Munk 1966), dom-
37 inated by the contribution in the Indo-Pacific sector. The upwelling in the circumpolar portion of
38 the domain and in the passive basin – the Pacific – is balanced by downwelling near the northern
39 end of the active basin – the Atlantic. This global circulation implies a transfer of intermediate
40 water from the passive into the active basin (with a transfer of deep water in the opposite direc-
41 tion). This transfer occurs in the circumpolar region, as detailed in Talley (2013) (there is also
42 a small exchange through the Bering Strait, which we neglect henceforth). The transfer of water
43 between the basins is geostrophically balanced at the southern boundary of each semi-enclosed
44 basin, requiring a difference in the depth of the isopycnals separating the intermediate and deep
45 waters at the eastern boundary of each basin. Specifically, these isopycnals are deeper in the South
46 Pacific than in the South Atlantic in the present day MOC as noted by Reid (1961). More recent
47 observations from the *World Ocean Atlas* (Locarnini et al. 2006; Antonov et al. 2006) confirm that
48 isopycnals near 1000m depth are shallower in the Atlantic than in the Indo-Pacific (see figure 1).
49 The strength of the inter basin flow is set by the amount of Ekman transport and the upwelling
50 into the intermediate waters of the Indo-Pacific. The interbasin transfer is only one component of
51 the total transport that forms the upper branch of the MOC: in addition to the interbasin flow, the
52 MOC, or more precisely the residual overturning circulation (ROC), must carry all of the Ekman

53 transport that occurs along the northern boundary of the Antarctic Circumpolar Current (ACC)
54 region, minus the eddy-flux of buoyancy at this boundary, as well as the diapycnal upwelling in
55 the Atlantic.

56 The mechanism for size-dependent interbasin transport is illustrated here by considering a gen-
57 eralization of the model by Gnanadesikan (1999) to two basins connected by a circumpolar region.
58 A geostrophically balanced interbasin flow, ψ_g , which transfers water from the passive basin to the
59 active basin, is necessary to satisfy the buoyancy budget (as shown in figure 2). The depth of the
60 intermediate water layer must be deeper in the passive basin than in the active basin in order to
61 geostrophically balance the interbasin flow. The transfer from the passive to the active basin is
62 fed by diffusive upwelling and Ekman transport into the passive basin, and therefore the transfer
63 is larger when the passive basin is wider. This simple model does not capture the richness of the
64 horizontal and vertical structure of the ROC velocity field, spanning both the active and the passive
65 basins, which we diagnose from three-dimensional numerical integrations.

66 These three-dimensional integrations follow the approach of Hughes and Weaver (1994) and
67 Marotzke and Willebrand (1991), that is we use an ocean-only model with drastically simplified
68 geometry and forcing. There is a two-basin geometry in which the latitudinal extent of the two
69 basins is the same. In this, we differ from the basic configuration of Hughes and Weaver (1994),
70 who specified that the Atlantic-like basin extends further north than the Pacific-like basin. The
71 purpose of our configuration is to determine the consequences of differences in the longitudinal
72 extent of the Atlantic- and Pacific-like basins. We confine our analysis to the weakly diffusive
73 regime, where the ROC has a substantial adiabatic component associated with the wind-driven
74 upwelling in the circumpolar portion of the domain (Toggweiler and Samuels 1993; Wolfe and
75 Cessi 2010).

76 The partition of the MOC between the Atlantic and Indo-Pacific sector in an idealized do-
77 main was also studied by Stocker and Wright (1991), using a zonally averaged model, with a
78 parametrization relating the East-West pressure gradient to the North-South one. They found that
79 under zonally symmetric forcing, the system settles into a state with two separate overturning cells
80 with sinking at the northern edge of both the North Atlantic and the North Pacific, and little transfer
81 between the two basins. Some ocean-only studies (Seidov and Haupt 2005) find that it is neces-
82 sary to impose an asymmetry in the surface salinity or freshwater flux to achieve a conveyor-like
83 global overturning circulation, while others find that multiple states exist depending on the initial
84 conditions (Huisman et al. 2009). Nilsson et al. (2013) find that in a coupled model, conveyor-like
85 states exist (in which sinking occurs in only one basin) as well as a northern-sinking state (in
86 which sinking occurs in the north of both basins). In the quasi-adiabatic regime, we find that under
87 longitudinally symmetric forcing, stable sinking is obtained only at the northern end of the nar-
88 row basin, a state which maximizes the inter-basin exchange of the ROC. No other states exist for
89 symmetric forcing. In order to achieve sinking in the wide basin, the surface forcing is modified
90 to decrease precipitation over the wide basin. The interbasin transport ψ_g in each of these states
91 compares well to the predictions of the two-basin zonally-average model.

92 Section 2 proposes an idealized zonally average model adapted from Gnanadesikan (1999). The
93 numerical model setup and some of the diagnostics are described in section 3. Section 4 describes
94 the numerical model states and section 5 illustrates the horizontal structure of the flow in the ROC.
95 A summary and concluding remarks are given in section 6.

96 **2. A minimal model of two basins exchanging transport**

97 Here, we consider an extension of Gnanadesikan (1999) model of the ROC to two basins coupled
98 by a circumpolar connection, as sketched in figures 2 and 3. This model is very similar to that

99 developed in Allison (2009); however in that model the lengths of the boundaries are different. It
 100 crudely captures the circulation in the upper branch of the ROC; the upper branch is defined to
 101 be the layer above the isopycnal b_m , that divides the intermediate water from the deep water. In
 102 the context of this model, the layer above b_m is referred to as the upper layer and the layer below
 103 b_m is referred to as the lower layer. Thickness is transferred between the layers through northern
 104 sinking, diapycnal upwelling, Ekman and eddy fluxes.

105 From figure 2, we can see that the buoyancy budget of the upper layer for the semienclosed
 106 portions of each basin is given by

$$\psi_{Ek}^a - \psi_{ed}^a + \psi_{\kappa}^a + \psi_g = \psi_N, \quad (1)$$

$$\psi_{Ek}^p - \psi_{ed}^p + \psi_{\kappa}^p - \psi_g = 0, \quad (2)$$

107 where ψ_{Ek} denotes the Ekman transport entering the basins from the circumpolar region, ψ_{ed} is the
 108 transport of buoyancy by eddy fluxes southward into the channel region (modeled here using the
 109 Gent-McWilliams parametrization: see section 3), ψ_{κ} is a diapycnal exchange of buoyancy across
 110 the isopycnal b_m , ψ_g is the geostrophically balanced exchange that results from the difference in
 111 zonal flow in the two sectors of the circumpolar domain and ψ_N is the transport due to sinking at
 112 the northern edge of the domain. We choose to explore the special case in which sinking ψ_N only
 113 occurs in one basin or the other. The superscripts “ a ” and “ p ” refer to the active and passive basins
 114 respectively.

115 In this model the depth of the isopycnal b_m is given by h_a in the active basin and h_p in the
 116 passive basin, as shown in figure 3. Following Gnanadesikan (1999), we can substitute standard
 117 expressions for Ekman, eddy, diapycnal and geostrophic transports into equations (1,2), to arrive

118 at the system

$$-\underbrace{\frac{\tau_s L_a}{\rho_0 f_s}}_{\psi_{Ek}^a} - \underbrace{\frac{\kappa_{GM} h_a L_a}{L_c}}_{\psi_{ed}^a} + \underbrace{\frac{\kappa A_a}{h_a}}_{\psi_{\kappa}^a} - \underbrace{\frac{g'(h_p^2 - h_a^2)}{2f_s}}_{\psi_g} = g' \frac{h_a^2}{2f_n}, \quad (3)$$

$$-\underbrace{\frac{\tau_s L_p}{\rho_0 f_s}}_{\psi_{Ek}^p} - \underbrace{\frac{\kappa_{GM} h_p L_p}{L_c}}_{\psi_{ed}^a} + \underbrace{\frac{\kappa A_p}{h_p}}_{\psi_{\kappa}^p} + \underbrace{\frac{g'(h_p^2 - h_a^2)}{2f_s}}_{\psi_g} = 0. \quad (4)$$

119 We have denoted the widths of the basins with $L_{a,p}$, τ_s is the wind-stress that drives Ekman trans-
 120 port out of the re-entrant channel, f_s is the Coriolis parameter at the southern boundary of the
 121 semi-enclosed portion of the domain, f_n is the Coriolis parameter at 57.5°N, L_C is the merid-
 122 ional extent of the circumpolar channel, κ_{GM} is the coefficient of Gent-McWilliams eddy-fluxes
 123 parametrization, κ is the interior diapycnal diffusivity, $A_{a,p}$ is the area of the semi-enclosed basins,
 124 g' is the range of surface buoyancies shared by the sinking and circumpolar regions. τ_s is the av-
 125 erage wind-stress along the northern-most closed barotropic streamline in the circumpolar region.
 126 This is the most appropriate definition of the northern edge of the re-entrant channel (Marshall
 127 et al. 2016). The values of the prescribed parameters are given in table 1.

128 The novel term here is the geostrophic transport ψ_g exchanged between the two basins, propor-
 129 tional to the difference between the squared heights of the upper layer at the eastern boundaries of
 130 each basin. At the southern edge of the semi-enclosed region, the height of the upper layer at the
 131 eastern boundary of one basin must be equal to the height of the upper layer at the western bound-
 132 ary of the other basin, in order to ensure no normal flow into the southern edge of the continent.
 133 In the system (3,4) we identify the characteristic depth of the isopycnal b_m in each basin with its
 134 depth at the eastern boundary. Therefore the geostrophic transport ψ_g into the upper layer of the
 135 active basin is proportional to the squared height of the upper layer at the eastern edge of the active
 136 basin, h_a , minus the squared height of the upper layer at the eastern edge of the passive basin, h_p .
 137 The geostrophic transport into the passive basin is $-\psi_g$, because the two heights are switched.

138 The system (3,4) can be solved for $h_{a,p}$, given the external parameters for geometry, forcing and
 139 diffusion. With the formulation (3,4), sinking in the narrow basin and sinking in the wide basin
 140 can be studied by simply exchanging the values of L_a, A_a with L_p, A_p .

141 Taking the sum of (3) and (4), ψ_g cancels out and we find

$$\psi_{Ek}^a - \psi_{ed}^a + \psi_{Ek}^p - \psi_{ed}^p + \psi_{\kappa}^a + \psi_{\kappa}^p = \psi_N. \quad (5)$$

142 Assuming that the difference in isopycnal heights is small compared with their total depth, i.e.
 143 $h_p = h_a + \epsilon$, with $\epsilon \ll h_a$, it is clear that the total amount of sinking ψ_N is, to leading order in ϵ , the
 144 same as that obtained in a single basin whose width is $L_a + L_p$ and whose area is $A_a + A_p$. In the
 145 same limit, the difference in isopycnal heights, $\epsilon \equiv h_p - h_a$, is given by

$$\epsilon \left[\frac{\kappa_{GM}}{L_c} + \frac{\kappa L_c}{h_a^2} + \frac{g' h_a (L_a + L_p)}{L_a L_p |f_s|} \right] = g' \frac{h_a^2}{2 f_n L_a}. \quad (6)$$

146 This shows that $\epsilon > 0$, i.e. the isopycnal b_m is always deeper in the passive basin, because the term
 147 inside the square bracket on the left hand side (lhs) of (6) is always positive, as is the right hand
 148 side (rhs). In addition (6) shows that ϵ and ψ_g are larger when sinking occurs in the narrow basin:
 149 if we exchange L_a with L_p , the term inside the square bracket on the lhs remains the same, while
 150 the rhs decreases. The resulting depths, $h_{a,p}$, and associated transport for sinking in the narrow
 151 or wide basin are given in table 2, for the parameters used listed in table 1. We choose the cases
 152 $L_a = 2L_p$ and $L_p = 2L_a$. However, it is of interest to note that if $A_a \rightarrow 0$, $h_a \sim h_p / \sqrt{2}$ and when
 153 $A_p \rightarrow 0$, $h_a \sim h_p$.

154 The essential point is that sinking in the narrow basin leads to a larger inter-basin flow, and
 155 a larger residual circulation per unit width, than sinking in the wide basin. The reason for this
 156 asymmetry is simple: if sinking occurs in the narrow basin then all of the residual flow entering
 157 the upper layer in the wide basin, through Ekman transport (minus the eddy contribution) and
 158 diapycnal mixing, must enter the narrow basin to sink, adding to the Ekman transport directly

159 entering the active basin. Regardless of the location of sinking the residual transport is given by
160 the sum of the Ekman transport at the northern edge of the channel (minus the eddy transport), and
161 the diapycnal upwelling throughout both basins. Thus, the transport *per unit width*, is larger when
162 sinking occurs in the narrow basin.

163 In the following section the predictions of this simple box model are examined with a three-
164 dimensional primitive equation GCM.

165 **3. Model and diagnostics**

166 The numerical model employed is the Massachusetts Institute of Technology general circulation
167 model (MITgcm, Marshall et al. 1997a,b), which integrates the hydrostatic, Boussinesq primitive
168 equations. The domain is a spherical sector spanning 140° in latitude and 210° in longitude with a
169 1° horizontal resolution. The geometrical configuration comprises two idealized basins, one twice
170 as wide as the other, joined by a re-entrant channel of latitudinal width 17.5° at the southern edge
171 of the domain as shown in Figure 4. The bottom is flat and 4000m deep, except for a sill in the
172 periodic channel, one-grid point wide and 1333m high, located immediately south of the narrow
173 basin's western boundary.¹ There are 32 unequally spaced levels in the vertical, ranging from a
174 minimum spacing of 13.6m at the top to a maximum of 286m at the bottom.

175 The equation of state is linear, so that the buoyancy is described by

$$b = g[\alpha_T T - \beta_S (S - S_{ref})], \quad (7)$$

176 where $\alpha_T = 2 \times 10^{-4} \text{ }^\circ\text{C}^{-1}$, $\beta_S = 7.4 \times 10^{-4}$ and $S_{ref} = 35$. Salinity is given on the practical salinity
177 scale and therefore it is quoted without units.

¹The experiments described here have been repeated in a domain with two sills, one at the southern end of each boundary. The qualitative properties of these experiments are the same, confirming that the sill does not cause the preference for narrow basin sinking.

178 The surface forcings are steady and zonally-uniform: the expressions for the wind stress, τ ,
 179 freshwater flux, F , and distribution to which the surface temperature is relaxed, T^* are given by

$$\tau = \tau_{Max} \left(-\cos(3\pi\theta/140) + 1.1e^{-\theta^2/2\sigma^2} \right), \quad (8)$$

$$F = F_{s0} \left(\cos(7\pi\theta/8\Theta) - 2e^{-(\theta/\Theta)^2/(2\sigma_F^2)} \right) - F_0, \quad (9)$$

$$T^* = T_{eq} \left(\cos(\pi\theta/140)^2 + 0.1e^{-(\theta/2\Theta-1)^2} \right). \quad (10)$$

180 We adopt the following notation: θ is latitude in $^\circ$, $\tau_{Max} = 0.11$ Pa, $\sigma = 10^\circ$, $F_{s0} = 2 \times 10^{-8}$ ms^{-1} ,
 181 $\sigma_F = 0.128$, $\Theta = 60^\circ$ and $T_{eq} = 25^\circ\text{C}$. The relaxation time-scale for the surface temperature is
 182 10 days. The constant F_0 is defined such that the area averaged freshwater flux $\langle F \rangle = 0$. The
 183 freshwater flux is then turned into a virtual salt flux by multiplying F by -35 . The distributions of
 184 τ , F , and T^* as a function of latitude are shown in figure 5.

185 Momentum is dissipated via Laplacian viscosity with horizontal and vertical coefficients
 186 $\nu_h = 4 \times 10^4$ $\text{m}^2 \text{s}^{-1}$ and $\nu_v = 1 \times 10^{-4}$ $\text{m}^2 \text{s}^{-1}$, respectively; we employ no-slip sidewalls and a
 187 free-slip bottom augmented by a linear bottom drag with coefficient $r = 3.5 \times 10^{-6}$ s^{-1} applied
 188 over the bottom grid cell. Because of the coarse model resolution, baroclinic eddies are parame-
 189 terized using the advective form of Gent and McWilliams (1990, hereafter GM) and Redi (1982)
 190 isopycnal mixing with equal mixing coefficients $K_{GM} = 500$ $\text{m}^2 \text{s}^{-1}$. GM is implemented using the
 191 boundary value problem scheme of Ferrari et al. (2010) with vertical mode number $m = 2$ and min-
 192 imum wavespeed $c_{\min} = 0.1$ m s^{-1} . The Redi tensor is tapered exponentially to horizontal diffusion
 193 in regions of weak stratification using the method of Danabasoglu and McWilliams (1995).

194 Tracers are advected using the second-order-moments (SOM) scheme of Prather (1986) and
 195 diffused using a vertical diffusivity, κ , which is surface intensified to mimic an idealized mixed
 196 layer such that

$$\kappa = \kappa_v + \kappa_m(1 + \tanh(z+d)/d), \quad (11)$$

197 where $\kappa_v = 2 \times 10^{-5} \text{ m}^2 \text{ s}^{-1}$, $\kappa_m = 10^{-2} \text{ m}^2 \text{ s}^{-1}$ and $d = 20 \text{ m}$.

198 *a. Residual overturning streamfunction*

199 The overturning circulation is quantified using the zonally integrated residual overturning
200 streamfunction (cf. Wolfe and Cessi, 2015)

$$\psi(y, \tilde{b}) \equiv \frac{1}{T} \int_0^T \int_0^{L_x} \int_{-H}^0 v^\dagger \mathcal{H}[b(x, y, z, t) - \tilde{b}] dz dx dt, \quad (12)$$

201 where $T = 100$ years, $v^\dagger = v + v_{\text{GM}}$ is the total meridional velocity (the sum of the resolved velocity
202 v and the eddy velocity from the GM parameterization v_{GM}), and \mathcal{H} is the Heaviside step function.

203 ψ is the zonally integrated transport of water above the isopycnal $b(x, y, z, t) = \tilde{b}$. The “vertical”
204 coordinate \tilde{b} is buoyancy; the tilde distinguishes the coordinate “buoyancy” from the buoyancy
205 field.

206 For presentation purposes, ψ is remapped into height coordinates using the mean isopycnal
207 height

$$\zeta(y, \tilde{b}) \equiv -\frac{1}{T} \int_0^T \frac{1}{L_x} \int_0^{L_x} \int_{-H}^0 \mathcal{H}[b(x, y, z, t) - \tilde{b}] dz dx dt. \quad (13)$$

208 In height coordinates, ψ advects a modified buoyancy $b^\sharp(y, z)$ that satisfies $\zeta[y, b^\sharp(y, z)] = z$; that is,
209 ψ is constant on b^\sharp contours for purely adiabatic flow.

210 Because of zonal buoyancy gradients, the remapping distorts the vertical extent of the mixed
211 layer. Buoyancies higher than $40 \times 10^{-3} \text{ m}^2 \text{ s}^{-1}$ are not plotted because the contours are too close
212 together.

213 **4. Pacific and Atlantic overturnings**

214 With the forcing in figure 5, the model settles into a narrow-sinking state where sinking occurs
215 at the northern end of the narrow basin. The resulting overturning circulation is shown in Figure 6

216 (colors and gray contours), together with b^\sharp (black contours). The maximum ψ is 15 Sv near
217 the northern end of the narrow basin and the interhemispheric circulation is quasi-adiabatic: the
218 northward flow at intermediate depths follows isopycnals fairly well in the southern hemisphere,
219 while the quasi-adiabatic residual flow in the northern hemisphere is augmented by a diffusively-
220 driven positive cell. The circulation has the same pattern as estimates of observed transport for
221 upper, intermediate and deep water (Talley et al. 2011), but the transports from the model shown
222 here are about 30% smaller than observed transports, because the maximum wind-stress in the
223 southern hemisphere is about half of the value observed in nature, and the domain is only 210°
224 wide. The deep overturning in the wide basin is characterized by two weak diffusively-driven
225 counter-rotating cells each confined to a single hemisphere with maximum residual transport of
226 about 6Sv.

227 We also force a wide-sinking circulation with sinking in the wide basin and upwelling in the
228 narrow basin. This is achieved by decreasing the freshwater flux in the Northern Hemisphere
229 of the wide basin by about 0.06Sv, with a corresponding uniform increase elsewhere, until the
230 circulation reverses (figure 7). Even though the active basin for wide sinking is twice as big as
231 the active basin for narrow sinking, the amplitude of the ROC is about the same in the two cases,
232 in agreement with the simple model described earlier. Once a new steady state is achieved, the
233 freshwater flux can be brought back to the symmetric profile shown in figure 5, and eventually, in
234 about 3000 years, the circulation reverts to sinking in the narrow basin.

235 In addition to the thickness weighted average fields as a function of latitude and buoyancy, we
236 consider the cumulative transports above a given buoyancy surface, which are a good measure of
237 the bulk transport by the upper branch of the overturning. The bounding buoyancy surface, b_m , is
238 chosen to be 0.0076 m s^{-2} : this choice captures most of the transport of the intermediate water cell,
239 while avoiding the diffusive abyssal cell (which forms only small amounts of bottom water in this

240 model). The zonally averaged position of this surface is shown by the thick black lines in figures
241 6 and 7, and its height as a function of latitude and longitude is shown in figure 8 for both narrow
242 sinking (top panels) and wide sinking (bottom panels). It is clear that the isopycnals, especially
243 at the eastern boundary, are shallower in the active basin. This is consistent with the results of
244 the simple model (table 2), and with observations, which show that neutral density surfaces with
245 maximum depths of around 1000m are deeper in the Indo-Pacific than in the Atlantic (figure 1).

246 In the channel, the barotropic flow has a wave-like structure that is asymmetric between basins.
247 Therefore, to illustrate the transports in the narrow and wide sectors of the southern part of the
248 domain, it is best to use a pseudo-streamwise horizontal coordinate system, which follows the
249 barotropic streamlines, Ψ , near the channel edge and relaxes to latitude circles both near the south-
250 ern boundary of the domain, and into the basin (32S is the latitude chosen). This tapering is nec-
251 essary to avoid closed contours in the streamlines of Ψ , which would make the coordinate system
252 unusable. Contours of the pseudo-streamwise coordinate system are shown in figure 9. This coor-
253 dinate system allows us to visualize the across-stream transport in each sector by considering the
254 divergence out of a volume bounded by an isopycnal and the surface in the vertical direction, by
255 the southern boundary and a barotropic streamline in the meridional direction, by the longitudes
256 of the western and eastern boundaries of the narrow and wide sectors in the zonal direction. To
257 calculate the across-stream transport, it is easier and numerically more accurate to integrate the
258 horizontal divergence of the vertically integrated velocity over a surface in the latitude longitude
259 plane as shown in figure 9 and use Gauss's theorem. In order for vector calculus to be valid in this
260 context, it is necessary to introduce a dual set of non-orthogonal unit vectors (Young 2012) such

261 that

$$\mathbf{e}^1 = \hat{\mathbf{i}} \quad \text{and} \quad \mathbf{e}^2 = \nabla\Psi \quad (14)$$

$$\mathbf{e}_1 = \frac{\Psi_y \hat{\mathbf{i}} - \Psi_x \hat{\mathbf{j}}}{\Psi_y} \quad \text{and} \quad \mathbf{e}_2 = \frac{\hat{\mathbf{j}}}{\Psi_y}. \quad (15)$$

262 The velocity divergence can then be calculated in the coordinate system most appropriate for the
263 model's output and this gives the result:

$$\int_{A(\Psi)} \nabla \cdot \mathbf{u} dA = \int_{C(\Psi)} \mathbf{u} \cdot \mathbf{e}^2 dl - \int_{-L}^{y(\Psi)} \mathbf{u} \cdot \mathbf{e}^1 dy \Big|_{left} + \int_{-L}^{y(\Psi)} \mathbf{u} \cdot \mathbf{e}^1 dy \Big|_{right}. \quad (16)$$

264 where $\mathbf{u} = u^1 \mathbf{e}_1 + v^1 \mathbf{e}_2 = u\hat{\mathbf{i}} + v\hat{\mathbf{j}}$. The northward transport across the barotropic streamline seg-
265 ment $C(\Psi)$ is balanced by the zonal transport of the *east-west* velocity (and not the along-stream
266 velocity), as well as the small diapycnal velocity associated with the area-integrated horizontal
267 divergence.

268 The cross-stream transport is then taken to be the first term on the right hand side of (16) and
269 is shown in figure 10, where the equivalent latitude is defined to span the same area enclosed by
270 $A(\Psi)$ within each sector. North of 32S the meridional transport is plotted instead.

271 The transports shown in figure 10 can be interpreted in the context of the simple model. There is
272 more diffusive upwelling in the wide basin than in the narrow basin and by volume conservation,
273 $\left(\int \int_{-h}^0 v dz dx \right)_y = \int w dx$, so the gradient of the lines in figure 10 is bigger for the wide basin than
274 for the narrow basin. In the simple model, it is assumed that in the northern hemisphere of each
275 basin, the diffusive upwelling north of the equator is balanced by buoyancy-driven sinking at the
276 northern end of the basin. Therefore ψ_N for the MITgcm simulations should be measured at the
277 equator. About 12Sv of transport crosses the equator in the active basin of both the narrow-sinking
278 and wide-sinking states. Table 2 compares the results of the numerical study to the simple model
279 described in section 2.

280 South of the edge of the semi-enclosed basin, the pressure and buoyancy is continuous in lon-
281 gitude. The difference in eastern boundary isopycnal heights at the southern edge of the basins
282 leads to an east-west height difference within each basin. This difference is associated with the
283 geostrophically balanced meridional transport ψ_g at the northern edge of the channel, which is out
284 of the passive basin and into the active basin. At the latitude where the continental boundaries ter-
285minate, the meridional exchange velocity turns from meridional to zonal in a narrow quasi-zonal
286 jet connecting the two basins. The transport through 0E and 70E/140W is shown in figure 11. In
287 both the narrow-sinking and wide-sinking states, the flow in the channel is westward, but there
288 is a difference in transport between the eastern and western sides of the active basin, due to this
289 quasi-zonal jet. The exchange flow ψ_g causes the transport on the western side of the active basin
290 to be larger by 8.2Sv in the case of narrow sinking, but only 3.1Sv in the case of wide sinking.

291 There are three important differences between the narrow-sinking and wide-sinking states il-
292 lustrated here: 1) Although the width of the wide basin is twice that of the narrow basin, the
293 wide-sinking ROC is only slightly bigger than the narrow-sinking ROC (figure 10); 2) The net
294 zonal inflow in the circumpolar region is from the wide to the narrow basin in the narrow-sinking
295 ROC and opposite in the wide-sinking ROC (cf. the difference between the zonal transport enter-
296 ing at the western boundary and the flow exiting at the eastern boundary in figure 11); 3) The net
297 zonal flow exchanged between the two basins is *larger* for the narrow-sinking ROC. The difference
298 in the zonal flows at the southern edges of the basins is associated with a change in the depths of
299 isopycnals at the eastern boundaries: an example of this difference in depths is shown in figure 8.

300 **5. Horizontal structure of the flow**

301 The zonally averaged view of the upper branch of the ROC hides the rich zonal structure of the
302 flow, which is strongly shaped by the wind-driven gyres. In figure 12, to visualize the horizontal

303 distribution of the ROC, we contour the streamfunction associated with the zonal transport above
 304 the isopycnal b_m (shown by a thick line in figures 6 and 7). The streamfunction is obtained by
 305 integrating the vertically integrated zonal transport northward starting from the southern boundary
 306 of the domain. The flow is horizontally divergent due to diapycnal flow in the interior and in
 307 the outcrop regions, so not all of the ROC transport is captured. This view of the ROC clearly
 308 shows the exchange flow between the two basins, highlighted by thick contours in figure 12. The
 309 exchange flow exits the passive basin on the western boundary, immediately turns east in a narrow
 310 zonal jet and enters the active basin on the western boundary. From there, the wind-driven gyres
 311 induce large-scale meanders, modulating the meridional transport into alternating broad flows
 312 around the anti-clockwise gyres and narrow western boundary currents to the west of clockwise
 313 gyres. Finally the exchange flow sinks in the north-east sector of the active basin. Comparing
 314 narrow-basin sinking with wide-basin sinking is it clear that the exchange flow is less in the latter
 315 case, but the pathways are qualitatively similar.

316 To visualize all of the transport, including the horizontally divergent portion, figure 13 shows
 317 the contours of a pseudo-streamline, ϕ_d , constructed by adding the diapycnal contribution to the
 318 integrated zonal transport, that is

$$\phi_d = - \int_{-L}^y d\hat{y} \left[U(x, \hat{y}) - \int_0^x d\hat{x} \varpi(\hat{x}, \hat{y}) \right], \quad (17)$$

319 where U is the zonal transport above the isopycnal b_m , and ϖ is the diapycnal velocity across the
 320 same isopycnal. This construction gives some apparent flow through the solid boundaries, but it
 321 has the advantage of illustrating the contribution of all the components of the ROC. In particular
 322 it shows that the ROC in the active basin is primarily connected to the diffusive overturning in the
 323 southern hemisphere of the active basin, while the northern hemisphere of the passive basin does
 324 not participate in the upper branch, in accordance with the zonally averaged view of figures 6 and

325 7. In both views of the flow, the meridional “throughflow” velocity in the regions of anti-clockwise
326 circulation is larger for narrow-basin sinking.

327 To characterize the lower branch of the ROC, a streamfunction is constructed by integrating the
328 zonal transport between b_m and the bottom. The streamlines thus obtained are shown in figure 14.
329 In the active basin the exchange flow is almost entirely confined to the western boundary, except
330 at the southern boundary of the basin, where it turns into a quasi-zonal flow before entering the
331 passive basin at the eastern boundary, and at the boundary between the subpolar and subtropical
332 gyres, where excursions in the interior occur, as observed by Bower et al. (2009). The interior
333 flow in the active basin is a mixture of the classical Stommel-Arons poleward flow, modified by
334 the wind-driven gyres, more prominently so in the wide basin, where the wind-gyres are stronger.
335 The view of the return flow of the ROC offered by ϕ_d (not shown), defined in (17), shows that the
336 meridional connection between the two basins does not extend to the northern hemisphere of the
337 passive basin, as already seen in figures 6, 7 and 13.

338 Finally, the three dimensional structure of the ROC can be partially visualized using particle
339 trajectories. Figure 15 shows the paths of particles that are initialized at the surface at the northern
340 edge of the channel in the passive sector. The particle trajectories shown are chosen to highlight
341 the path of the Ekman transport ψ_{Ek}^P as it enters the passive basin, turns, and becomes the interbasin
342 flow ψ_g which flows around the continental boundary and into the active basin. The particles ini-
343 tially move northward in the Ekman layer, then are subducted in the passive basin, getting caught
344 in both the tropical and subtropical gyres. The particles do not cross the equator in the passive
345 basin, but move approximately adiabatically into the active basin. There, they go northward until
346 they sink in the north-east part of the sub polar gyre. The transit-time from entering the active
347 basin to the sinking location is highly dependent on particle initialization: particle transit-time
348 varies with the depth of the particle and with the number of times it goes around in the gyres. In

349 figure 15, the transit-time from the channel to the sinking location is 125yrs for the narrow sinking
350 case and about 175yrs for the wide sinking case.

351 **6. Conclusions**

352 In a two-basin simplified configuration of the world ocean, with one wide and one narrow basin
353 connected by a re-entrant channel, the meridional overturning circulation prefers a state with sink-
354 ing at the northern edge of the narrow basin balanced by upwelling elsewhere. The salt-advection
355 feedback reinforces this preference. A wide-sinking circulation with sinking at the northern edge
356 of the wide basin can be coerced by imposing reduced freshwater flux in this region, but this state is
357 unstable to forcing that is zonally symmetric. The exchange flow between the basins is maximized
358 in the narrow-basin sinking state, leading to a larger average depth of intermediate isopycnals in
359 the passive versus the active basin. This difference in isopycnal depths between basins results in a
360 higher sea surface height in the passive basin compared to the active basin.

361 The total residual transport is essentially fixed by the strength of the wind-stress and the eddies
362 in the ACC, and by the diapycnal upwelling into the upper branch of the ROC. These quantities
363 are approximately independent of the location of the sinking: if sinking were to occur in the North
364 Pacific rather than the North Atlantic, the strength of the ROC transport would be about the same,
365 even though the Indo-Pacific is much larger than the Atlantic. Consequently, the transport per
366 unit width, or the typical meridional velocity associated with the upper (and lower) branch of the
367 ROC would be smaller for North Pacific sinking compared to North Atlantic sinking, unless the
368 meridional transport is all concentrated in a narrow boundary current.

369 The approximate independence of the ROC transport on the sinking location implies that the
370 through-flow velocity is faster when sinking occurs in the narrow basin. In addition, a plan view
371 of the upper branch of the overturning circulation reveals that the northward path of the ROC

372 “snakes” around the gyres. When passing clockwise gyres, the overturning streamlines follow
373 the western boundary, and so the velocity on these streamlines is high and there is little time for
374 exchange of salinity with the atmosphere. When passing anti-clockwise gyres, the streamlines
375 move to the eastern side of the gyre and the flow is slower so there is more time for exchange
376 of salinity with the atmosphere. The complexities of the three dimensional circulation may be
377 important in setting the distribution of tracers, especially salinity, which strongly controls the range
378 of surface buoyancy shared between the sinking region and the upwelling region in the circumpolar
379 current. Maximizing this range of shared buoyancies allows efficient adiabatic transport along the
380 isopycnals connecting the two hemispheres. Further analysis of the implications of this flow field
381 to tracer transport is deferred to a subsequent study.

382 *Acknowledgments.* CSJ and PC are supported by the National Science Foundation under Grant
383 No. OCE-1258887 and the Office of Science (BER), U.S. Department of Energy, under Grant
384 No. DE-SC0005100. Computational resources were provided by XSEDE consortium, which is
385 supported by National Science Foundation Grant ACI-1053575. Thanks go to Jinbo Wang, who
386 contributed the particle trajectory code.

387 **References**

- 388 Allison, L. C., 2009: Spin-up and adjustment of the antarctic circumpolar current and global
389 pycnocline. Ph.D. thesis, University of Reading.
- 390 Antonov, J. I., R. A. Locarnini, T. P. Boyer, A. V. Mishonov, and H. E. Garcia, 2006: *World Ocean*
391 *Atlas 2005, Volume 2: Salinity*. U.S. Government Printing Office, Washington, D.C., 182 pp.
- 392 Bower, A. S., M. S. Lozier, S. F. Gary, and C. W. Boning, 2009: Interior pathways of the
393 north atlantic meridional overturning circulation. *Nature*, **459 (7244)**, 243–247, doi:10.1038/

394 nature07979.

395 Danabasoglu, G., and J. C. McWilliams, 1995: Sensitivity of the global ocean circulation to pa-
396 rameterizations of mesoscale tracer transports. *J. Climate*, **8** (12), 2967–2987.

397 Ferrari, R., S. M. Griffies, A. J. G. Nurser, and G. K. Vallis, 2010: A boundary-value problem
398 for the parameterized mesoscale eddy transport. *Ocean Modell.*, **32**, 143–156, doi:10.1016/j.
399 ocemod.2010.01.004.

400 Gent, P. R., and J. C. McWilliams, 1990: Isopycnal mixing in ocean circulation models. *J. Phys.*
401 *Oceanogr.*, **20**, 150–155, doi:10.1175/1520-0485(1990)020<0150:IMIOCM>2.0.CO;2.

402 Gnanadesikan, A., 1999: A simple predictive model for the structure of the oceanic pycnocline.
403 *Science*, **283**, 2077–2079, doi:10.1126/science.283.5410.2077.

404 Hughes, T. M. C., and A. J. Weaver, 1994: Multiple equilibria of an asymmetric two-basin
405 ocean model. *J. Phys. Oceanogr.*, **24** (3), 619–637, doi:10.1175/1520-0485(1994)024<0619:
406 MEOAAT>2.0.CO;2.

407 Huisman, S., H. A. Dijkstra, A. von der Heydt, and W. P. M. de Ruijter, 2009: Robustness of
408 multiple equilibria in the global ocean circulation. *Geophys. Res. Lett.*, **36**, L01 610.

409 Locarnini, R. A., A. V. Mishonov, J. I. Antonov, T. P. Boyer, and H. E. Garcia, 2006: *World Ocean*
410 *Atlas 2005, Volume 1: Temperature*. U.S. Government Printing Office, Washington, D.C., 182
411 pp.

412 Marotzke, J., and J. Willebrand, 1991: Multiple equilibria of the global thermohaline circulation.
413 *J. Phys. Oceanogr.*, **21** (9), 1372–1385, doi:10.1175/1520-0485(1991)021<1372:MEOTGT>2.
414 0.CO;2.

- 415 Marshall, D. P., R. D. Munday, L. C. Allison, R. J. Hay, and H. L. Johnson, 2016: Gill's model
416 of the antarctic circumpolar current, revisited: The role of latitudinal variations in wind stress.
417 *Ocean Modelling*, **97**, 37–51, doi:10.1016/j.ocemod.2015.11.010.
- 418 Marshall, J., A. Adcroft, C. Hill, L. Perelman, and C. Heisey, 1997a: A finite-volume, incom-
419 pressible Navier Stokes model for studies of the ocean on parallel computers. *J. Geophys. Res.*,
420 **102 (C3)**, 5753–5766, doi:10.1029/96JC02775.
- 421 Marshall, J., C. Hill, L. Perelman, and A. Adcroft, 1997b: Hydrostatic, quasi-hydrostatic, and non-
422 hydrostatic ocean modeling. *J. Geophys. Res.*, **102 (C3)**, 5733–5752, doi:10.1029/96JC02776.
- 423 Munk, W. H., 1966: Abyssal recipes. *Deep Sea Res.*, **13**, 707–730.
- 424 Nilsson, J., P. L. Langen, D. Ferreira, and J. Marshall, 2013: Ocean basin geometry and the
425 salinification of the Atlantic Ocean. *J. Climate*, **26**, 6163–6184, doi:10.1175/JCLI-D-12-00358.
426 1.
- 427 Prather, M. J., 1986: Numerical advection by conservation of second-order moments. *J. Geophys.*
428 *Res.*, **91 (D6)**, 6671–6681, doi:10.1029/JD091iD06p06671.
- 429 Redi, M. H., 1982: Oceanic isopycnal mixing by coordinate rotation. *J. Phys. Oceanogr.*, **12**,
430 1154–1158, doi:10.1175/1520-0485(1982)012<1154:OIMBCR>2.0.CO;2.
- 431 Reid, J. L., 1961: On the temperature, salinity, and density differences between the atlantic and
432 pacific oceans in the upper kilometre. *Deep Sea Research (1953)*, **7 (4)**, 265 – 275, doi:doi:
433 10.1016/0146-6313(61)90044-2.
- 434 Seidov, D., and B. J. Haupt, 2005: How to run a minimalist's global ocean conveyor. *Geophysical*
435 *Research Letters*, **32 (7)**, doi:10.1029/2005GL022559.

- 436 Stocker, T. F., and D. G. Wright, 1991: A zonally averaged ocean model for the thermohaline cir-
437 culation. Part II: Interocean circulation in the Pacific-Atlantic basin system. *J. Phys. Oceanogr.*,
438 **21 (12)**, 1725–1739.
- 439 Stommel, H., and A. B. Arons, 1959: On the abyssal circulation of the world ocean—II. An
440 idealized model of the circulation pattern and amplitude in oceanic basins. *Deep Sea Res.*, **6**,
441 217–218, doi:10.1016/0146-6313(59)90075-9.
- 442 Talley, L. D., 2013: Closure of the global overturning circulation through the Indian, Pacific,
443 and Southern Oceans: Schematics and transports. *Oceanography*, **26 (1)**, 80–97, doi:10.5670/
444 oceanog.2013.07.
- 445 Talley, L. D., G. L. Pickard, W. J. Emery, and J. H. Swift, 2011: *Descriptive Physical Oceanogra-*
446 *phy: An Introduction*. 6th ed., Academic Press.
- 447 Toggweiler, J. R., and B. Samuels, 1993: Is the magnitude of the deep outflow from the Atlantic
448 Ocean actually governed by Southern Hemisphere winds? *The Global Carbon Cycle, NATO ASI*
449 *Ser., Ser. I*, M. Heimann, Ed., Springer, New York, 333–366, doi:10.1007/978-3-642-84608-3_
450 13.
- 451 Wolfe, C. L., and P. Cessi, 2010: What sets the strength of the mid-depth stratification and over-
452 turning circulation in eddying ocean models? *J. Phys. Oceanogr.*, **40 (7)**, 1520–1538, doi:
453 10.1175/2010JPO4393.1.
- 454 Young, W. R., 2012: An exact thickness-weighted average formulation of the Boussinesq equa-
455 tions. *J. Phys. Oceanogr.*, **42 (5)**, 692–707.

456 **LIST OF TABLES**

457 **Table 1.** The external parameters for the simplified two-basin transport budget, as de-
458 duced from the numerical simulations. 24

459 **Table 2.** Results of the simplified two-basin model, based on equations (3,4), compared
460 to the numerical MITgcm simulations. 25

Parameter	Value	Notes
κ_{GM}	$500\text{m}^2\text{s}^{-1}$	Value used in the numerical model.
L_p	10000km	Width of the wide basin at the channel edge.
L_a	5000km	Width of the narrow basin at the channel edge.
L_c	2000km	North-South extent of the channel.
A_a	$4 \times 10^{13}\text{m}^2$	Area of the narrow basin north of the channel and south of the equator.
A_p	$8 \times 10^{13}\text{m}^2$	Area of the wide basin north of the channel and south of the equator.
ρ_0	$1000\text{kg m}^3\text{s}^{-1}$	The average density.
$f_n = -f_s$	$1.2 \times 10^{-4}\text{s}^{-1}$	$ f $ at 57.5°S , the northern edge of the channel.
κ	$2 \times 10^{-5}\text{m}^2\text{s}^{-1}$	Value used in the numerical model.
τ	0.1	Average wind stress along the northernmost barotropic contour in the re-entrant channel
g'	0.004ms^{-2}	Approximate range of buoyancy shared between the channel and the northern end of the active basin.

461 TABLE 1. The external parameters for the simplified two-basin transport budget, as deduced from the numerical
462 simulations.

	Sinking in the narrow basin	MITgcm in narrow sinking	Sinking in the wide basin	MITgcm wide sinking
ψ_N	11.3Sv	11.8Sv	11.9Sv	11.9Sv
ψ_g	7.2Sv	8.2Sv	3.8Sv	3.1Sv
ψ_{Ek}^p	8.3Sv		4.2Sv	
ψ_{Ek}^a	4.2Sv		8.3Sv	
ψ_{ed}^p	2.6Sv		1.2Sv	
ψ_{ed}^a	1.0Sv		2.1Sv	
ψ_{κ}^p	1.5Sv		0.8Sv	
ψ_{κ}^a	1.0Sv		1.8Sv	
h_a	824m	841m	845m	821m
h_p	1055m	1016m	970m	882m

463 TABLE 2. Results of the simplified two-basin model, based on equations (3,4), compared to the numerical
464 MITgcm simulations.

LIST OF FIGURES

465		
466	Fig. 1.	Depth of three middepth neutral density γ_n surfaces as a function of latitude at three lon-
467		gitudes corresponding to the Atlantic (30°W), Indian (90°E), and Pacific (150°W) Oceans.
468		Lines that are the same color represent the same value of γ_n , whereas lines that are the same
469		style represent the same longitude. From Wolfe and Cessi (2010). 28
470	Fig. 2.	Schematic of the two-basin box model, showing the transport budget above the isopycnal
471		bounding the upper branch of the residual overturning circulation (ROC) for sinking in the
472		narrow basin (top) and wide basin (bottom). \otimes denotes sinking (transport from the upper
473		layer into the lower layer) and \ominus denotes upwelling (transport from the lower layer into the
474		upper layer). ψ_N represents northern sinking in the active basin, ψ_κ diapycnal upwelling,
475		ψ_{Ek} the Ekman transport at the northern edge of the channel region, ψ_{ed} the eddy-fluxes at
476		the northern edge of the channel region, and ψ_g a geostrophic exchange transport, which
477		flows out of the passive and into the active basin in the upper layer. 29
478	Fig. 3.	Schematic of the two-basin box model, showing the transport budget above the isopycnal
479		bounding the upper branch of the ROC for the active basin (top) and passive basin (bottom).
480		b_m is the isopycnal that divides the upper layer and the lower layer and $h_{a,p}$ denotes the
481		height of the upper layer. The other symbols are defined in figure 2. 30
482	Fig. 4.	Barotropic streamfunction and geometry of the domain used in the computations. The do-
483		main is 210°-periodic and 4000m deep. 31
484	Fig. 5.	Forcing fields as a function of latitude: wind-stress (top), relaxation temperature (middle),
485		freshwater flux (bottom). The dashed lines show the freshwater flux applied to induce a
486		sinking in the wide basin. Where these lines split, the upper dashed line is applied to the
487		narrow basin and the lower is applied to the wide basin. 32
488	Fig. 6.	Residual overturning streamfunction in Sverdrups (color contours, interval 2Sv), and
489		$b^\# \times 10^3 \text{ m s}^{-2}$, the buoyancy of the surface whose average depth is z (black contours) in the
490		narrow basin (top) and the wide basin (bottom). Sinking is in the narrow basin. In both plots,
491		the re-entrant channel region (left of the thick black dotted line) shows the total stream func-
492		tion over all longitudes. The thick black contour denotes the isopycnal $b_m = 0.0076 \text{ m s}^{-2}$
493		which bounds the upper branch of the ROC. 33
494	Fig. 7.	Residual overturning streamfunction in Sverdrups (color contours, interval 2Sv), and
495		$b^\# \times 10^3 \text{ m s}^{-2}$, the buoyancy of the surface whose average depth is z (black contours) in the
496		narrow basin (top) and the wide basin (bottom). Sinking is in the wide basin. In both plots,
497		the re-entrant channel region (left of the thick black dotted line) shows the total stream func-
498		tion over all longitudes. The thick black contour denotes the isopycnal $b_m = 0.0076 \text{ m s}^{-2}$
499		which bounds the upper branch of the ROC. 34
500	Fig. 8.	Contours of the height (m) of the isopycnal $b_m = 0.0076 \text{ m s}^{-2}$ for narrow-basin sinking
501		(top) (the thick black line in figure 6) and wide-basin sinking (bottom) (the thick black line
502		in figure 7). The domain is 210°-periodic: the western 20° of the wide basin is repeated to
503		the right of the figure. Contour interval is 50 m. 35
504	Fig. 9.	Contours of the pseudo-streamwise coordinate (Sv) used to evaluate the divergence of the
505		residual velocity for narrow-basin sinking (top) and wide-basin sinking (bottom). The con-
506		tours are constructed using the barotropic streamfunction between the thick contours, and
507		tapered to latitude circles to the north and south of the displayed area. The domain is
508		210°-periodic: the western 20° of the wide basin is repeated to the right of the figure. 36

509 **Fig. 10.** The zonally average thickness weighted meridional transports integrated above the isopycnal
510 $b = 0.0076 \text{ m s}^{-2}$ for narrow basin sinking (black lines) and wide basin sinking (grey lines).
511 The thin vertical line denotes the northern edge of the circumpolar region. 37

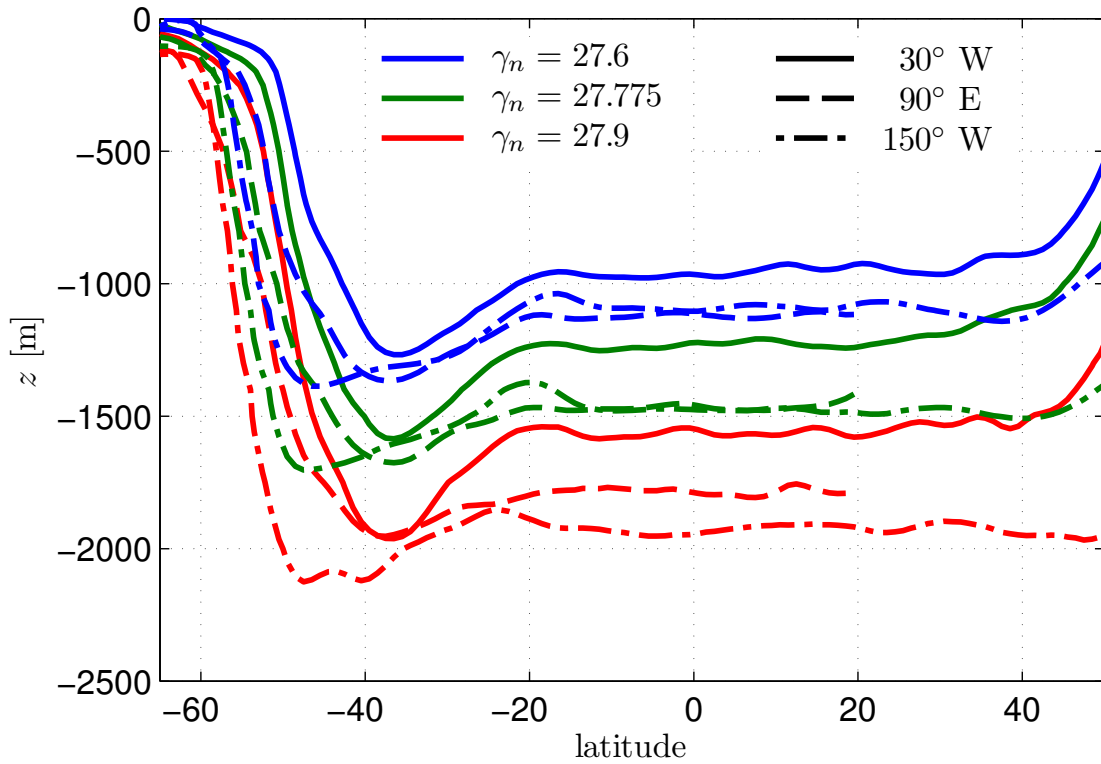
512 **Fig. 11.** Zonal transport, U , integrated above the isopycnal $b = 0.0076 \text{ m s}^{-2}$ at the eastern boundaries
513 of the wide basin (solid line) and the narrow basin (dashed line) and their difference (dashed-
514 dotted line) for narrow sinking (top) and wide sinking (bottom). The net difference in the
515 Atlantic sinking case is 8.2Sv (top) and in the Pacific sinking case it is -3.1Sv (bottom). 38

516 **Fig. 12.** Streamlines of the transport (Sv) above $b_m = 0.0076 \text{ m s}^{-2}$ for narrow-basin sinking (top) and
517 wide-basin sinking (bottom). The streamlines are constructed by integrating the thickness
518 weighted zonal flow in latitude. The contour interval is 8Sv for the thin lines and 2Sv for
519 the thick lines, which denote the interbasin exchange flow. Negative streamlines are dashed.
520 The domain is 210° -periodic: the western 20° of the wide basin is repeated to the right of
521 the figure. 39

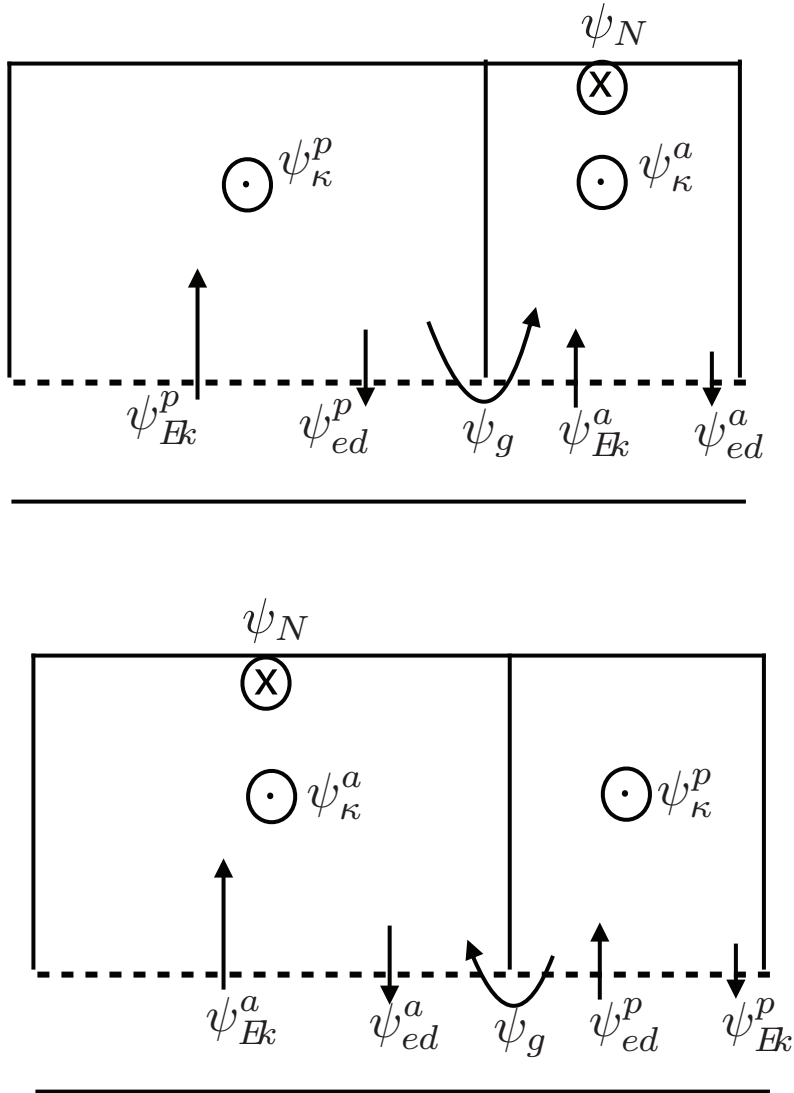
522 **Fig. 13.** Isolines of ϕ_d defined in (17) (Sv) for narrow-basin sinking (top) and wide-basin sinking
523 (bottom). The contour interval is 10 Sv for the thin lines and 2.5Sv for the thick lines,
524 which denote the interbasin exchange flow. Negative values of ϕ_d are dashed. The domain
525 is 210° -periodic: the western 20° of the wide basin is repeated to the right of the figure. 40

526 **Fig. 14.** Streamlines of the transport (Sv) between $b = 0.0076 \text{ m s}^{-2}$ and the bottom for narrow-basin
527 sinking (top) and wide-basin sinking (bottom). The streamline are constructed by integrating
528 the thickness weighted zonal flow in latitude. The contour interval is 8 Sv for the thin lines
529 and 2Sv for the thick lines, which denote the interbasin exchange flow. Negative streamlines
530 are dashed. 41

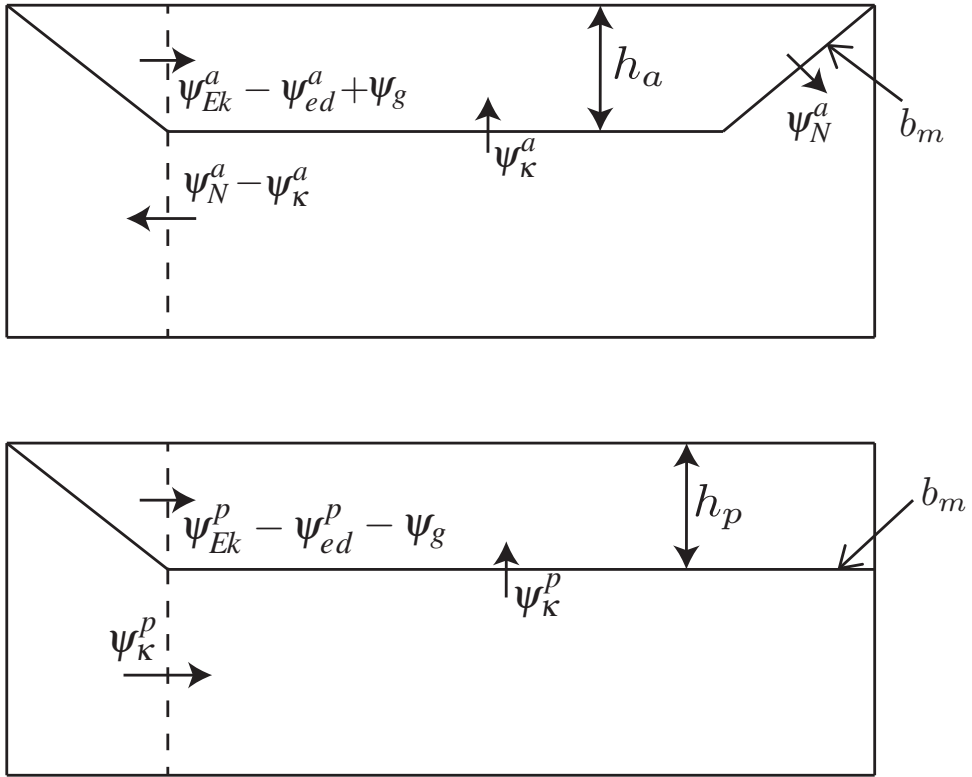
531 **Fig. 15.** The depth (m) of the isopycnal $b_m = 0.0076 \text{ m}^2 \text{ s}^{-1}$ is plotted in greyscale for narrow sinking
532 (top) and wide sinking (bottom). This isopycnal divides the upper branch of the ROC from
533 the lower branch. The location of the trajectory of a particle is shown in rainbow colors,
534 with one point plotted every 14 days, and the color indicates particle depth (m). The active
535 basin is plotted on the left in both cases, so that a continuous particle track is visible. The
536 particles are initialized at the surface and at the northern edge of the channel in the passive
537 sector. Trajectories that pass first into the passive basin and then into the active basin are
538 chosen. The domain is 210° -periodic. 42



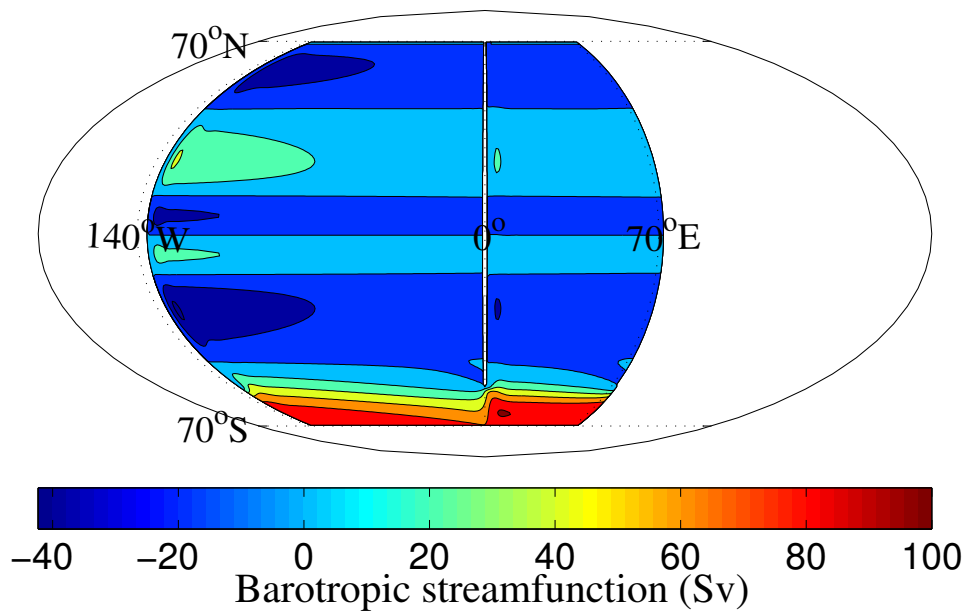
539 FIG. 1. Depth of three middepth neutral density γ_n surfaces as a function of latitude at three longitudes
 540 corresponding to the Atlantic (30°W), Indian (90°E), and Pacific (150°W) Oceans. Lines that are the same color
 541 represent the same value of γ_n , whereas lines that are the same style represent the same longitude. From Wolfe
 542 and Cessi (2010).



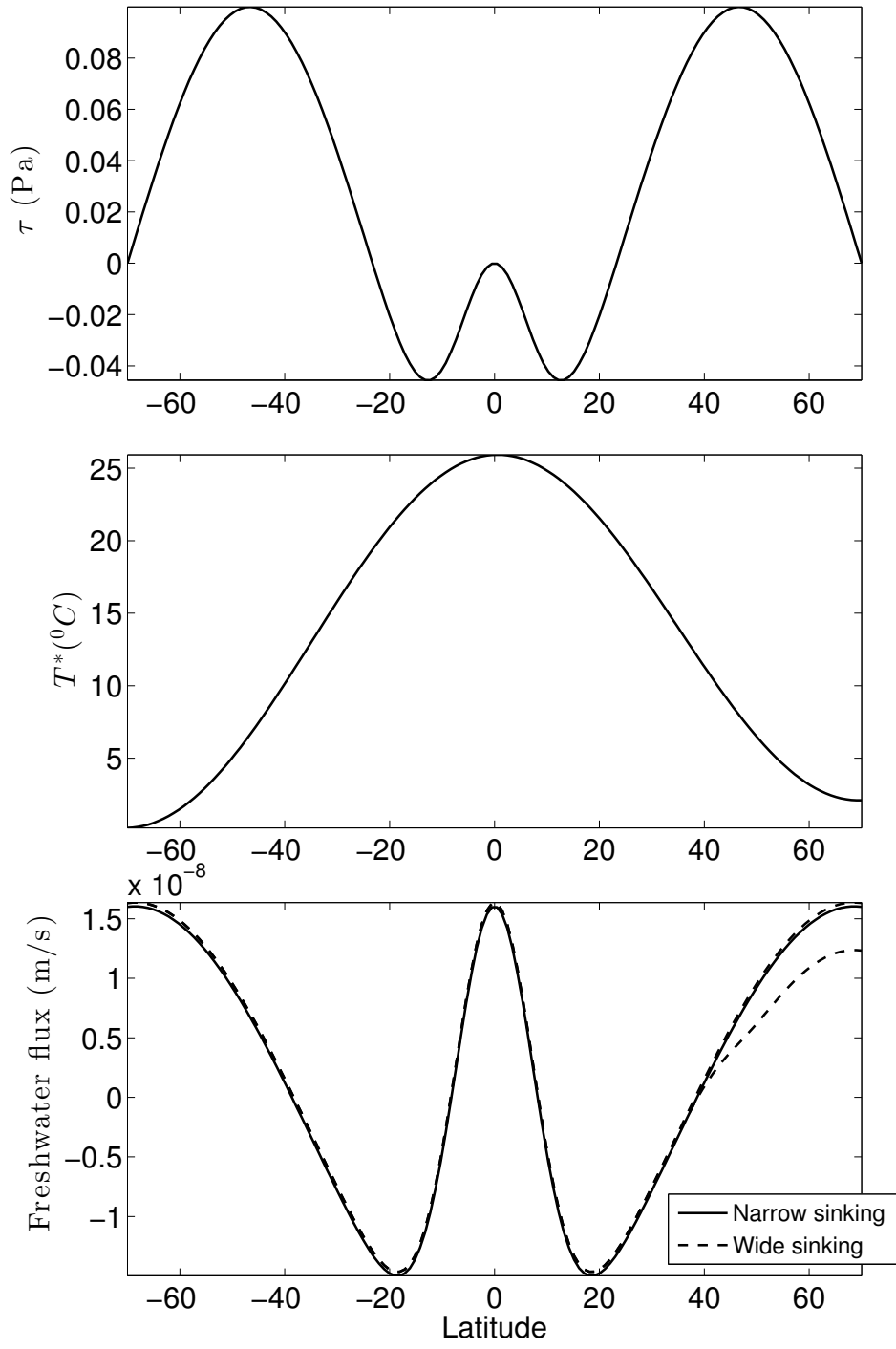
543 FIG. 2. Schematic of the two-basin box model, showing the transport budget above the isopycnal bounding
 544 the upper branch of the residual overturning circulation (ROC) for sinking in the narrow basin (top) and wide
 545 basin (bottom). \otimes denotes sinking (transport from the upper layer into the lower layer) and \odot denotes upwelling
 546 (transport from the lower layer into the upper layer). ψ_N represents northern sinking in the active basin, ψ_κ
 547 diapycnal upwelling, ψ_{Ek} the Ekman transport at the northern edge of the channel region, ψ_{ed} the eddy-fluxes at
 548 the northern edge of the channel region, and ψ_g a geostrophic exchange transport, which flows out of the passive
 549 and into the active basin in the upper layer.



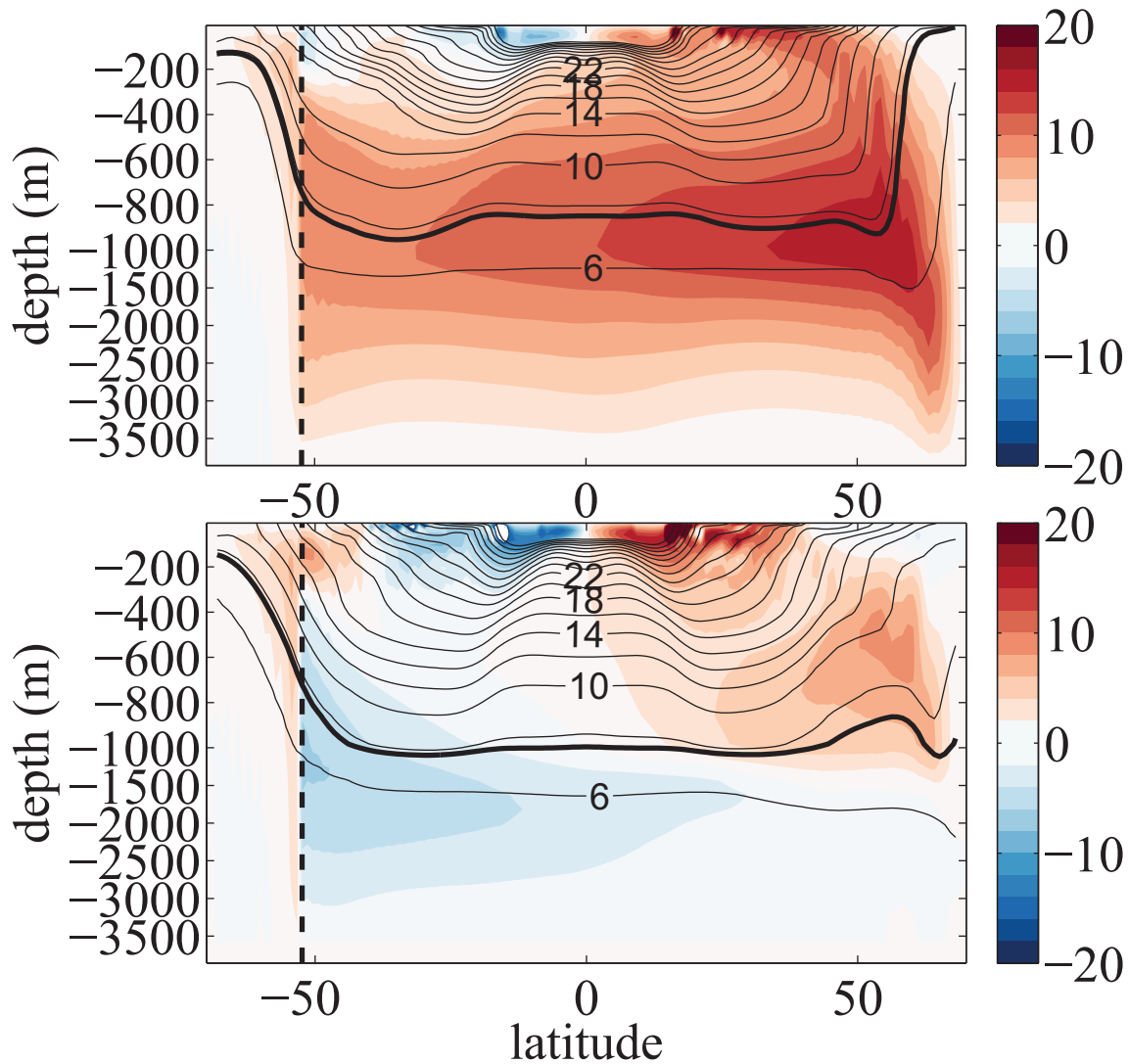
550 FIG. 3. Schematic of the two-basin box model, showing the transport budget above the isopycnal bounding the
 551 upper branch of the ROC for the active basin (top) and passive basin (bottom). b_m is the isopycnal that divides
 552 the upper layer and the lower layer and $h_{a,p}$ denotes the height of the upper layer. The other symbols are defined
 553 in figure 2.



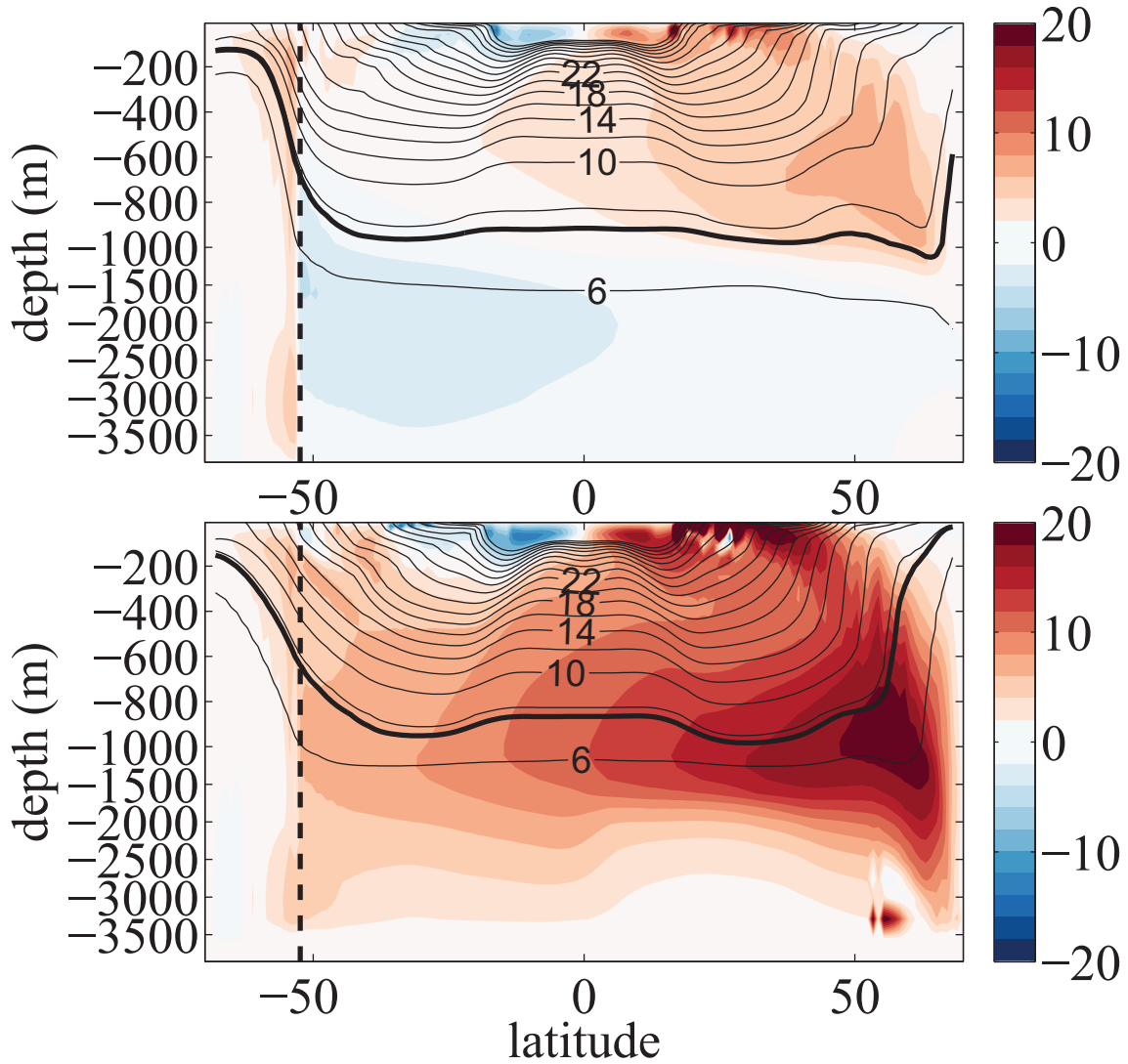
554 FIG. 4. Barotropic streamfunction and geometry of the domain used in the computations. The domain is
555 210°-periodic and 4000m deep.



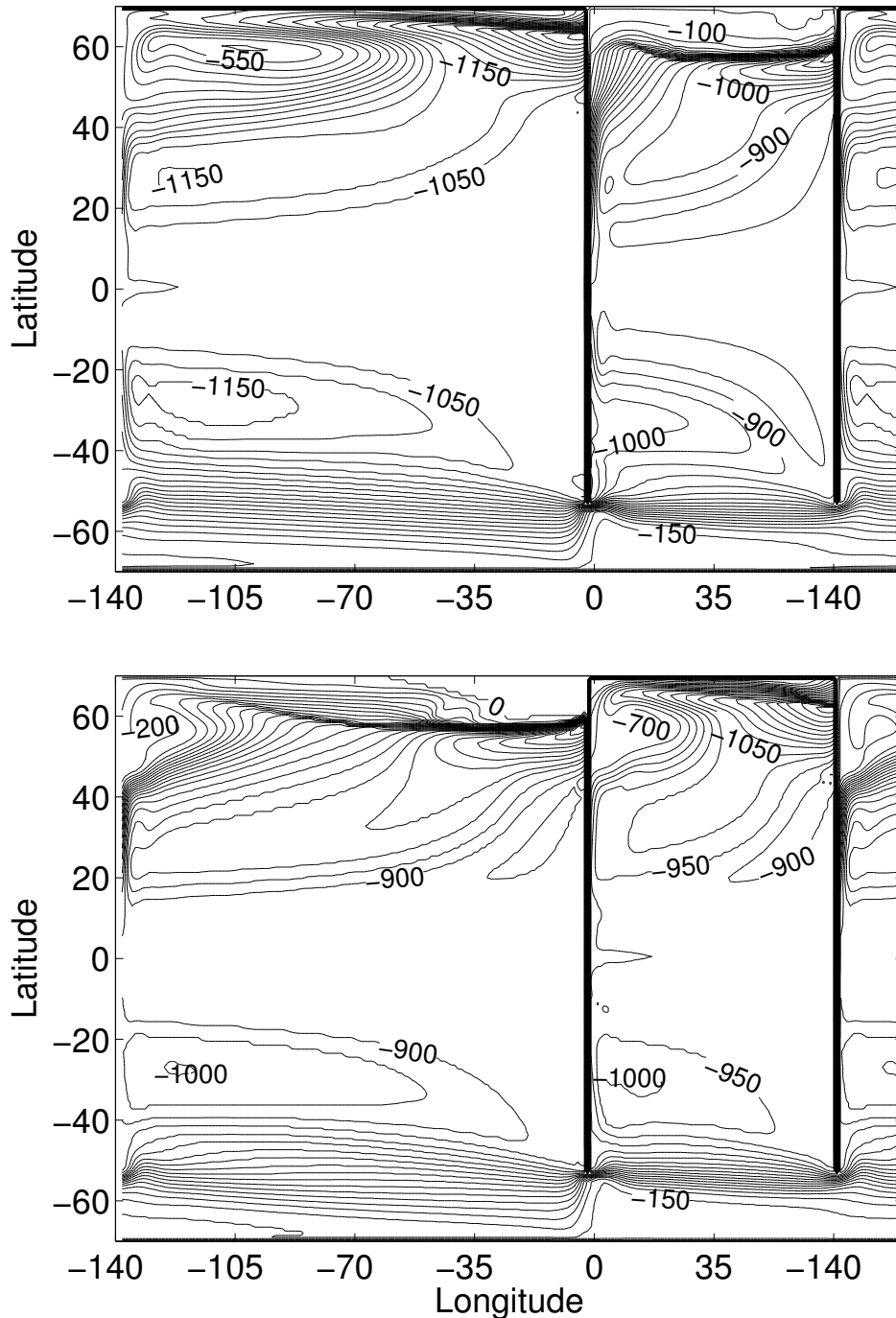
556 FIG. 5. Forcing fields as a function of latitude: wind-stress (top), relaxation temperature (middle), freshwater
 557 flux (bottom). The dashed lines show the freshwater flux applied to induce a sinking in the wide basin. Where
 558 these lines split, the upper dashed line is applied to the narrow basin and the lower is applied to the wide basin.



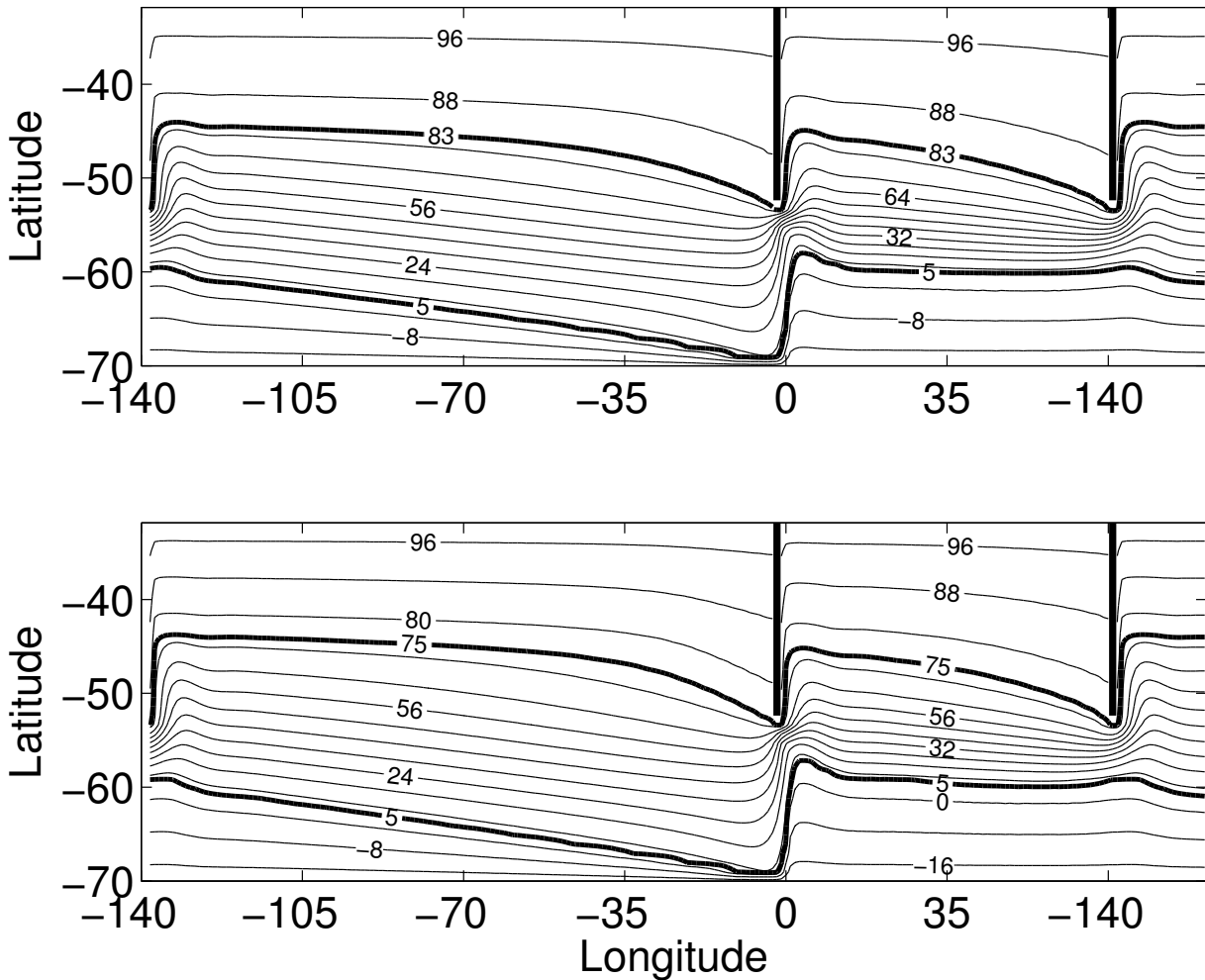
559 FIG. 6. Residual overturning streamfunction in Sverdrups (color contours, interval 2Sv), and $b^\# \times 10^3 \text{ m s}^{-2}$,
 560 the buoyancy of the surface whose average depth is z (black contours) in the narrow basin (top) and the wide
 561 basin (bottom). Sinking is in the narrow basin. In both plots, the re-entrant channel region (left of the thick black
 562 dotted line) shows the total stream function over all longitudes. The thick black contour denotes the isopycnal
 563 $b_m = 0.0076 \text{ m s}^{-2}$ which bounds the upper branch of the ROC.



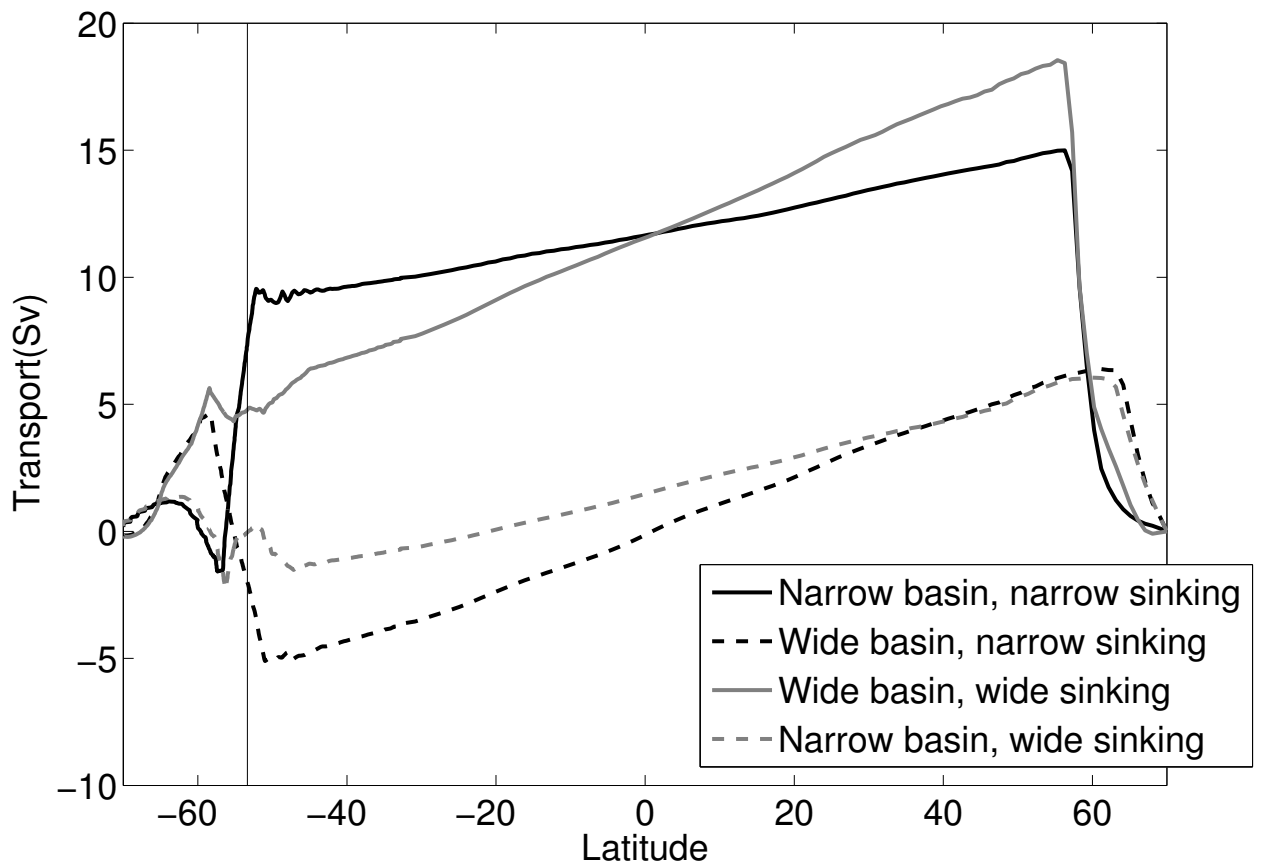
564 FIG. 7. Residual overturning streamfunction in Sverdrups (color contours, interval 2Sv), and $b^\# \times 10^3 \text{ m s}^{-2}$,
 565 the buoyancy of the surface whose average depth is z (black contours) in the narrow basin (top) and the wide
 566 basin (bottom). Sinking is in the wide basin. In both plots, the re-entrant channel region (left of the thick black
 567 dotted line) shows the total stream function over all longitudes. The thick black contour denotes the isopycnal
 568 $b_m = 0.0076 \text{ m s}^{-2}$ which bounds the upper branch of the ROC.



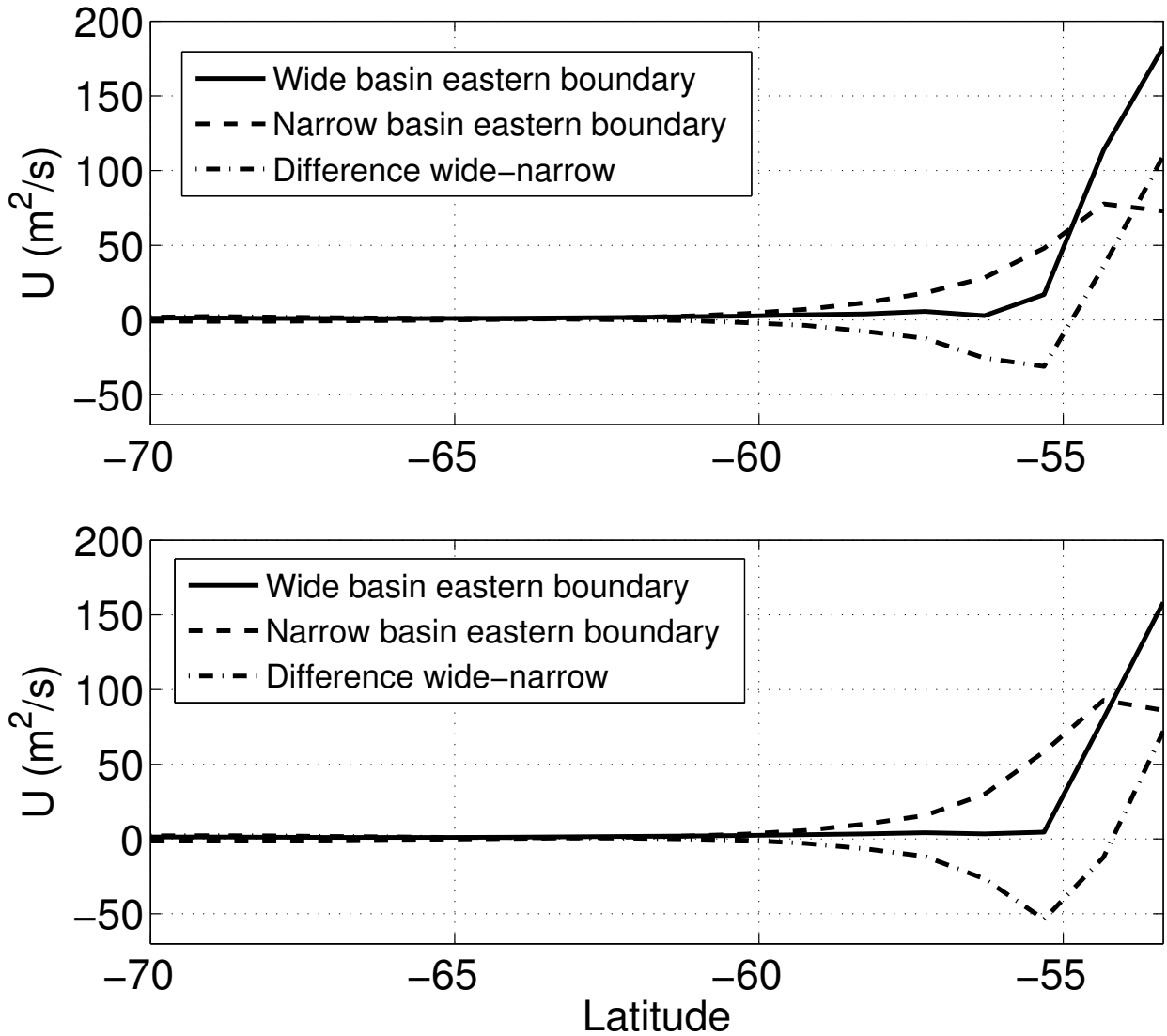
569 FIG. 8. Contours of the height (m) of the isopycnal $b_m = 0.0076 \text{ms}^{-2}$ for narrow-basin sinking (top) (the
 570 thick black line in figure 6) and wide-basin sinking (bottom) (the thick black line in figure 7). The domain is
 571 210° -periodic: the western 20° of the wide basin is repeated to the right of the figure. Contour interval is 50 m.



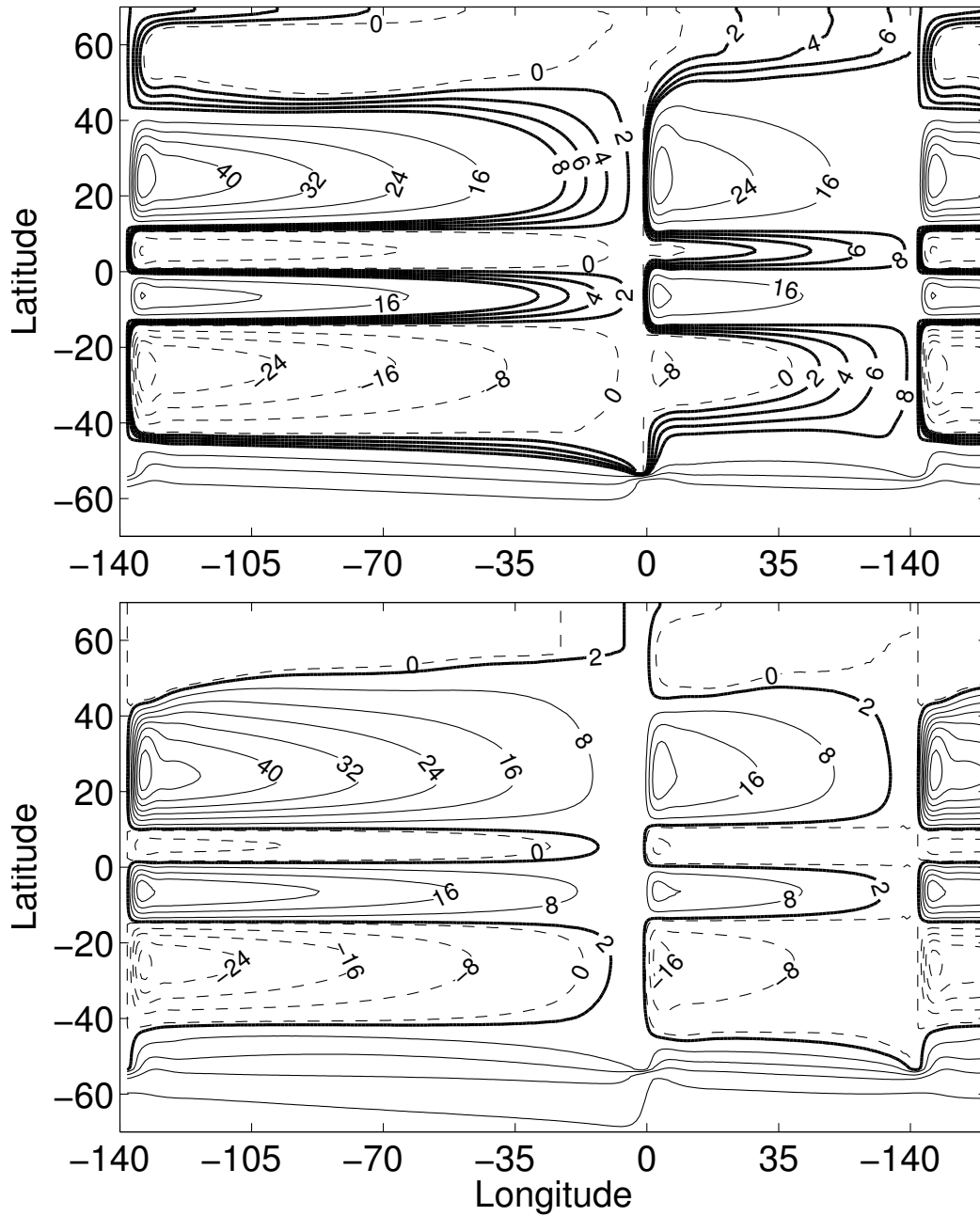
572 FIG. 9. Contours of the pseudo-streamwise coordinate (S_v) used to evaluate the divergence of the residual
 573 velocity for narrow-basin sinking (top) and wide-basin sinking (bottom). The contours are constructed using the
 574 barotropic streamfunction between the thick contours, and tapered to latitude circles to the north and south of
 575 the displayed area. The domain is 210° -periodic: the western 20° of the wide basin is repeated to the right of
 576 the figure.



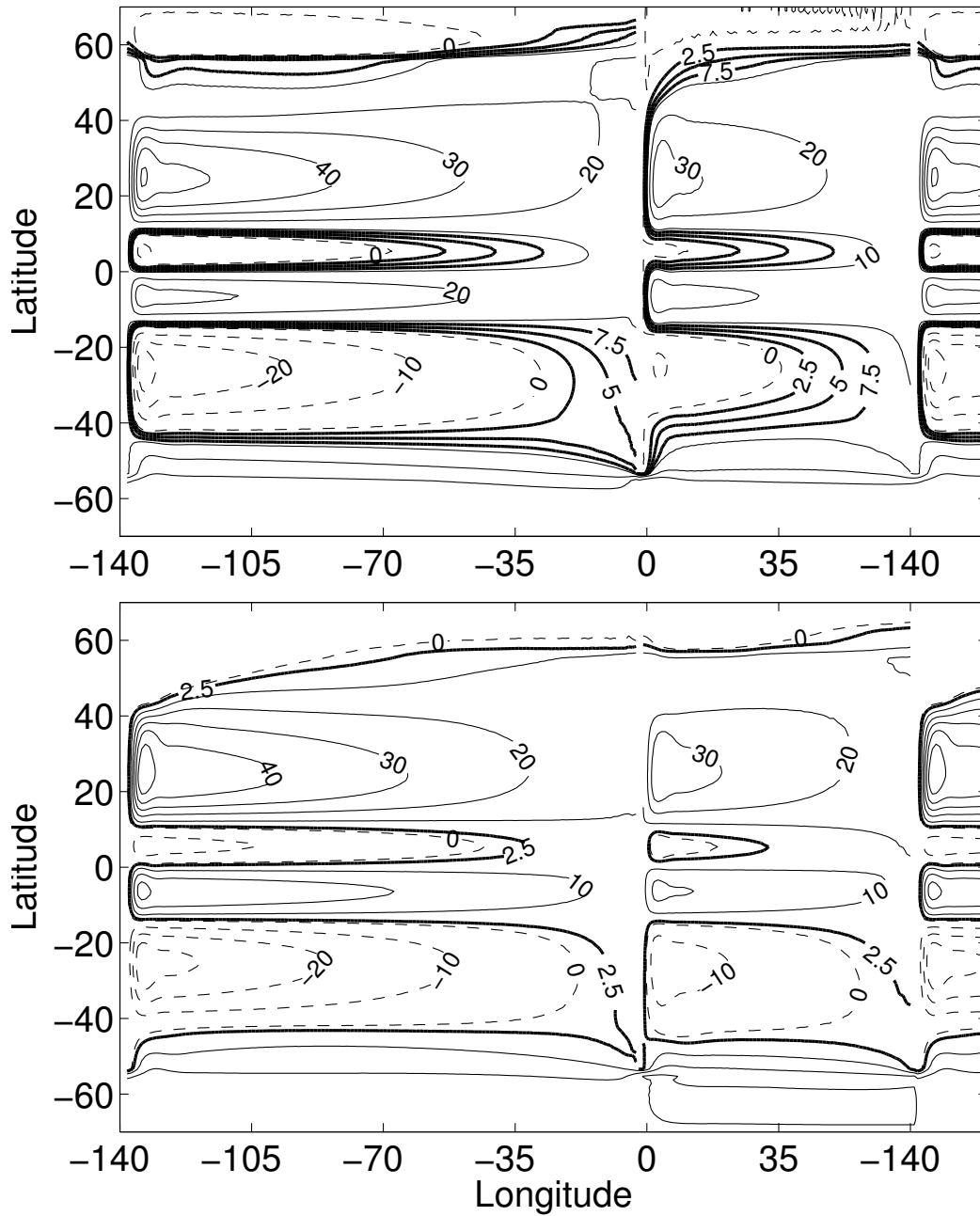
577 FIG. 10. The zonally average thickness weighted meridional transports integrated above the isopycnal
 578 $b = 0.0076 \text{ m s}^{-2}$ for narrow basin sinking (black lines) and wide basin sinking (grey lines). The thin vertical line
 579 denotes the northern edge of the circumpolar region.



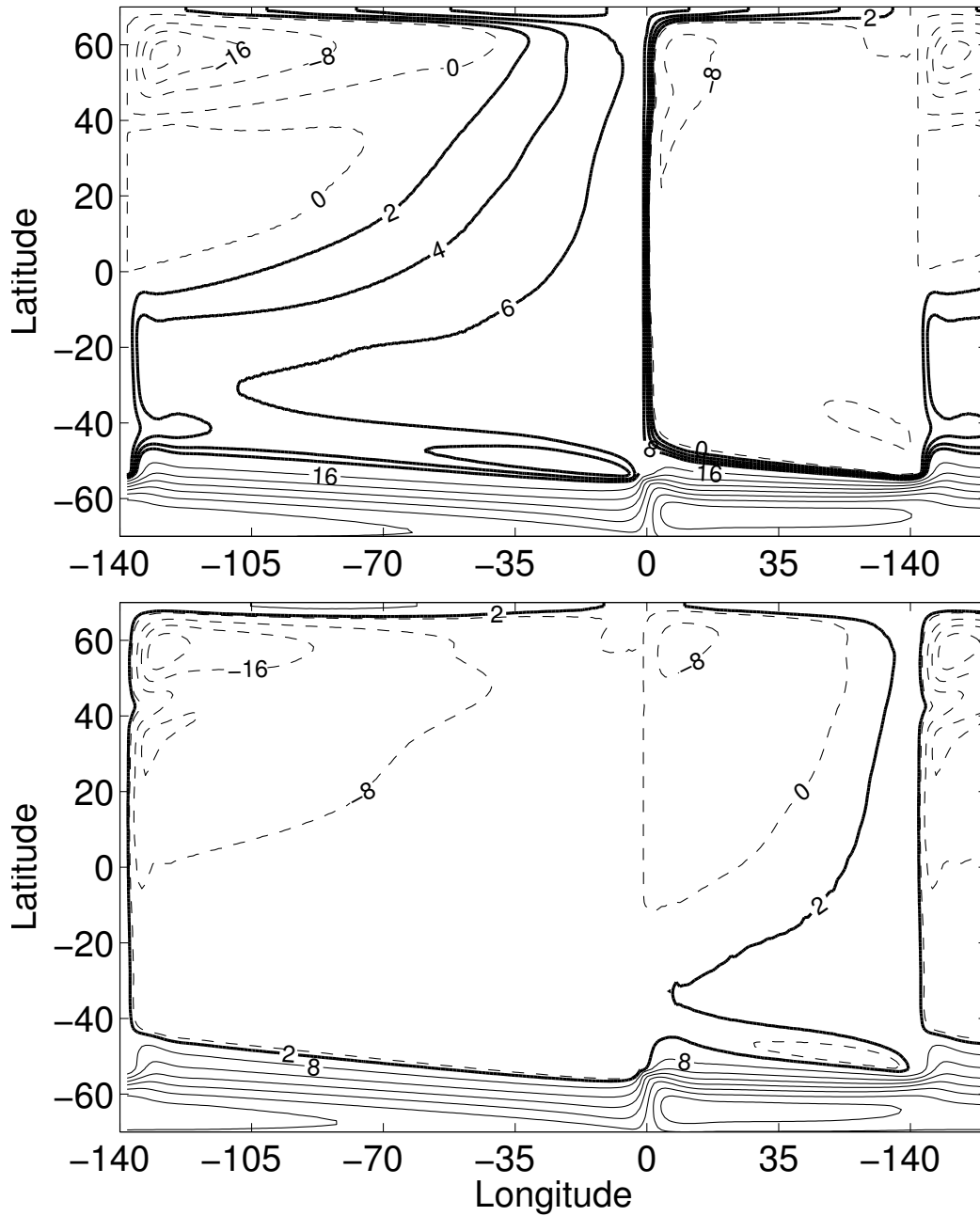
580 FIG. 11. Zonal transport, U , integrated above the isopycnal $b = 0.0076 \text{ m s}^{-2}$ at the eastern boundaries of the
 581 wide basin (solid line) and the narrow basin (dashed line) and their difference (dashed-dotted line) for narrow
 582 sinking (top) and wide sinking (bottom). The net difference in the Atlantic sinking case is 8.2 Sv (top) and in the
 583 Pacific sinking case it is -3.1 Sv (bottom).



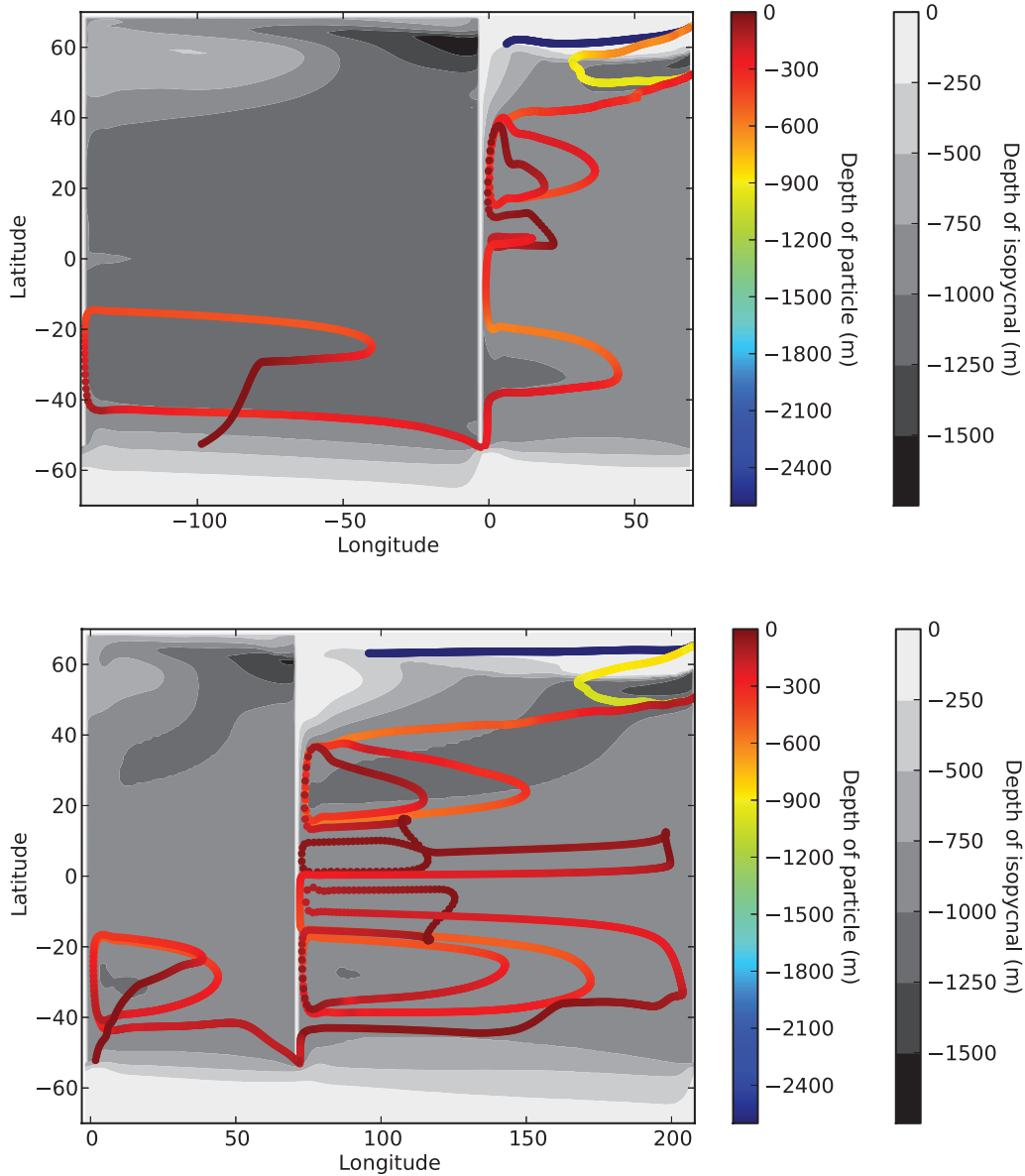
584 FIG. 12. Streamlines of the transport (Sv) above $b_m = 0.0076 \text{ m s}^{-2}$ for narrow-basin sinking (top) and wide-
 585 basin sinking (bottom). The streamlines are constructed by integrating the thickness weighted zonal flow in
 586 latitude. The contour interval is 8Sv for the thin lines and 2Sv for the thick lines, which denote the interbasin
 587 exchange flow. Negative streamlines are dashed. The domain is 210°-periodic: the western 20° of the wide
 588 basin is repeated to the right of the figure.



589 FIG. 13. Isolines of ϕ_d defined in (17) (Sv) for narrow-basin sinking (top) and wide-basin sinking (bottom).
 590 The contour interval is 10 Sv for the thin lines and 2.5Sv for the thick lines, which denote the interbasin exchange
 591 flow. Negative values of ϕ_d are dashed. The domain is 210° -periodic: the western 20° of the wide basin is
 592 repeated to the right of the figure.



593 FIG. 14. Streamlines of the transport (Sv) between $b = 0.0076 \text{ ms}^{-2}$ and the bottom for narrow-basin sinking
 594 (top) and wide-basin sinking (bottom). The streamlines are constructed by integrating the thickness weighted
 595 zonal flow in latitude. The contour interval is 8 Sv for the thin lines and 2Sv for the thick lines, which denote
 596 the interbasin exchange flow. Negative streamlines are dashed.



597 FIG. 15. The depth (m) of the isopycnal $b_m = 0.0076 \text{ m}^2 \text{ s}^{-1}$ is plotted in greyscale for narrow sinking (top) and
 598 wide sinking (bottom). This isopycnal divides the upper branch of the ROC from the lower branch. The location
 599 of the trajectory of a particle is shown in rainbow colors, with one point plotted every 14 days, and the color
 600 indicates particle depth (m). The active basin is plotted on the left in both cases, so that a continuous particle
 601 track is visible. The particles are initialized at the surface and at the northern edge of the channel in the passive
 602 sector. Trajectories that pass first into the passive basin and then into the active basin are chosen. The domain is
 603 210° -periodic.